

## ENGINEERING

# A fully biodegradable and self-electrified device for neuroregenerative medicine

Liu Wang<sup>1\*</sup>, Changfeng Lu<sup>2\*</sup>, Shuhui Yang<sup>1\*</sup>, Pengcheng Sun<sup>1\*</sup>, Yu Wang<sup>2†</sup>, Yanjun Guan<sup>2</sup>, Shuang Liu<sup>3</sup>, Dali Cheng<sup>4</sup>, Haoye Meng<sup>2</sup>, Qiang Wang<sup>4</sup>, Jianguo He<sup>1</sup>, Hanqing Hou<sup>3</sup>, Huo Li<sup>2</sup>, Wei Lu<sup>2</sup>, Yanxu Zhao<sup>2</sup>, Jing Wang<sup>2</sup>, Yaqiong Zhu<sup>2</sup>, Yunxuan Li<sup>1</sup>, Dong Luo<sup>2</sup>, Tong Li<sup>2</sup>, Hao Chen<sup>1</sup>, Shirong Wang<sup>5</sup>, Xing Sheng<sup>4</sup>, Wei Xiong<sup>3</sup>, Xiumei Wang<sup>1</sup>, Jiang Peng<sup>2†</sup>, Lan Yin<sup>1†</sup>

Peripheral nerve regeneration remains one of the greatest challenges in regenerative medicine. Deprivation of sensory and/or motor functions often occurs with severe injuries even treated by the most advanced microsurgical intervention. Although electrical stimulation represents an essential nonpharmacological therapy that proved to be beneficial for nerve regeneration, the postoperative delivery at surgical sites remains daunting. Here, a fully biodegradable, self-electrified, and miniaturized device composed of dissolvable galvanic cells on a biodegradable scaffold is achieved, which can offer both structural guidance and electrical cues for peripheral nerve regeneration. The electroactive device can provide sustained electrical stimuli beyond intraoperative window, which can promote calcium activity, repopulation of Schwann cells, and neurotrophic factors. Successful motor functional recovery is accomplished with the electroactive device in behaving rodent models. The presented materials options and device schemes provide important insights into self-powered electronic medicine that can be critical for various types of tissue regeneration and functional restoration.

## INTRODUCTION

Peripheral nerve injuries constitute ~2.8% of all trauma cases, affecting more than 1 million of people annually in the world and often leading to severe sensory deficits and/or impaired motor functions, which can have devastating impacts on patients' daily activities (1, 2). For repairing large lesion gaps (>1 cm), surgical interventions based on reconstructive grafting are usually necessary to bridge the nerve defects (3, 4). Currently, autologous nerve grafting (autograft) remains the most common and the standard solution for clinical treatments (5); however, full functional recovery can only be achieved for ~50% of patients, and the treatment suffers from inherent drawbacks, such as donor site morbidity, limited sources of donor nerves, mismatch between injured nerves and donor nerves, and the necessity of additional surgeries to obtain donor nerves (4, 6). Alternatively, tremendous efforts have been dedicated to develop bioartificial nerve grafts (or conduits) to guide neural growth. Explored materials are mostly based on biodegradable polymers that eliminate retrieval procedures after tissue regeneration, including both nature-derived materials (7) and synthetic polymers (7, 8). Bioactive cues can be incorporated with bioscaffolds to facilitate cell growth and enhance therapeutic effects. For example, pharmacological approaches including growth-promoting cells (8, 9) and/or growth factors (10, 11)

have been proposed to create a biologically and/or chemically active microenvironment (12).

Physical stimulations and electrical stimulations, in particular, are capable of delivering nonpharmacological therapies for restoring functions of impaired tissues and organs. Electrical signals have been proven to offer critical bioactive cues to promote neurite extension and accelerate nerve functional recovery (13–16). For example, Al-Majed *et al.* and other researchers have shown that electrical stimulations [alternating current (ac) or direct current (dc) electric fields] can accelerate the nerve outgrowth and functional recovery in rodents for several types of nerves, including sciatic nerves and facial nerves (13, 17–21); the neuronal differentiation of PC12 cells, neurite outgrowth of dorsal root ganglion (DRG) neurons, and neurotrophic factors released by Schwann cells could be promoted by ac or dc electric fields (22–25). The efficacy of electrical stimulation has also been identified to attenuate pain and accelerate axonal regeneration and target reinnervation in human subjects who suffer from carpal tunnel syndrome (26, 27). Despite the above advances, the effective delivery of postoperative electrical stimulation directly at surgical sites remains a daunting challenge. Enhanced therapeutic effects have been reported with multiple days of short-term electrical stimulation (28), suggesting the importance of delivering electrical stimulation beyond the intraoperative window. Currently available clinical treatments are limited to be within the intraoperative period or transcutaneous stimulations after index of surgical procedure, which constrains the operational time window. Precise transcutaneous electrical stimulation at the injury sites could also be challenging with possible infection risks. Recently proposed implantable electrical stimulation devices could potentially address these issues, e.g., wirelessly powered cuff electrodes have been proposed to promote sciatic nerve repair (29), nondegradable self-powered scaffolds based on glucose fuel cells have been shown to improve axonal growth (30), and bioresorbable wireless electrical stimulators via inductive coupling have been achieved to enhance the regeneration of transected nerves (28). Nevertheless, further advancements

<sup>1</sup>School of Materials Science and Engineering, The Key Laboratory of Advanced Materials of Ministry of Education, State Key Laboratory of New Ceramics and Fine Processing, Center for Flexible Electronics Technology, Tsinghua University, Beijing 100084, P. R. China. <sup>2</sup>Institute of Orthopedics, Chinese PLA General Hospital, Beijing 100853, P. R. China. <sup>3</sup>School of Life Sciences, IDG/McGovern Institute for Brain Research at Tsinghua University, Tsinghua University, Beijing 100084, P. R. China. <sup>4</sup>Department of Electronic Engineering, Beijing National Research Center for Information Science and Technology, and Beijing Innovation Center for Future Chips, Tsinghua University, Beijing 100084, P. R. China. <sup>5</sup>Beijing Advanced Innovation Center for Intelligent Robots and Systems, Beijing Institute of Technology, Beijing 100081, P. R. China.

\*These authors contributed equally to this work.

†Corresponding author. Email: lanyin@tsinghua.edu.cn (L.Y.); pengjiang301@126.com (J.P.); wangwangdian628@126.com (Y.W.)

on materials strategies and device schemes are desirable to facilitate postoperative electrical therapy and enhance therapeutic effects, as ideal device systems would prefer additional miniaturization, simplified fabrication processes, all biodegradable components to eliminate surgical retrieval, and operation without the use of external equipment for power delivery.

Here, we report a biodegradable, self-electrified, and ultraminiaurized conduit device for promoting peripheral nerve regeneration, which simultaneously offers structural guidance and sustained electrical cues in the biological systems without additional surgical complications. The electroactive microscale conduit device consists of dissolvable galvanic cells made of thin-film magnesium (Mg) and iron-manganese alloy (FeMn) electrodes on a polymer-based biodegradable scaffold. For cultured cells *in vitro*, the electroactive galvanic cells are shown to not only stimulate calcium activity and neurite outgrowth of DRG neurons but also promote the proliferation of Schwann cells and the up-regulation of neurotrophic factors. The implantable devices are used to treat transected sciatic nerve injuries (with 10-mm gaps) in Sprague-Dawley (SD) rats, demonstrating accelerated neuroregeneration and enhanced functional recovery *in vivo*. The entire device is fully biocompatible and biodegradable in physiological environments, eliminating secondary surgeries for retrieval. The materials options and device strategies provide new routes to exploit effective postoperative electrical therapy through biodegradable, self-powered, and miniaturized implants that can be critical for the function recovery of target tissues and organs.

## RESULTS AND DISCUSSION

### Materials strategies and device fabrication

Schematic structures of the fully biodegradable and self-electrified conduit appear in Fig. 1A, and the exploded illustration of each layer is given in Fig. 1B, with the fabrication process given in Fig. 1C. The device is composed of a dissolvable galvanic cell consisting of thin-film metallic electrodes embedded in a biodegradable nerve guidance conduit, which has a bilayer structure comprising porous polycaprolactone (PCL) and copolymer of poly(L-lactic acid) and poly(trimethylene carbonate) (PLLA-PTMC). Serving as the inner layer of the conduit, a flexible and highly stretchable PLLA-PTMC film (thickness,  $\sim 300\ \mu\text{m}$ ) is used to provide desirable interface for nerve tissues. Formed via a salt-etching method (Fig. 1C), the porous PCL film (thickness,  $\sim 350\ \mu\text{m}$ ) serves as the outer layer of the conduit, which not only provides the mechanical support against deformation induced by the surgical procedure and surrounding tissues but also ensures permeability of nutrition factors. Figure 1D shows the microstructure of porous PCL films with the internal pore diameters ranging from 20 to 40  $\mu\text{m}$ , determined by the size of sodium chloride particles used in the salt-etching process. Stacking the separately formed porous PCL and PLLA-PTMC films yields the bilayer conduit structure (Fig. 1C). The mechanical properties of porous PCL, PLLA-PTMC, and the bilayer structure are given in fig. S1.

Magnesium (Mg; thickness, 3.5  $\mu\text{m}$ ) and iron-manganese alloy (FeMn; thickness, 1.5  $\mu\text{m}$ ) thin films are deposited through magnetron sputtering (Fig. 1C), serving as water-soluble electrodes on each side of the conduit to form a galvanic cell that can provide sustained electric fields using body fluids as the electrolyte. Mg and FeMn are adopted as the anode and the cathode, respectively, because of their suitable electrochemical potential (31, 32), ideal biocompat-

ibility (33–35), and the desirable degradation rates in biological environments (36, 37). As necessary trace elements in the human body (34, 38), Mg has been adopted as stimulation electrodes at the nerve interface for nerve regeneration showing minimal toxicity (28), and Fe and Mn have been considered as biocompatible materials for cardiovascular stents (35, 39). It has been reported that the degradation rate of FeMn alloys [35 weight % (wt %) Mn] could be about three times higher than that of pure Fe (37). In addition, the antiferromagnetic character of FeMn alloys with Mn > 29 wt % can offer ideal compatibility with magnetic resonance imaging (MRI) and magnetron sputtering techniques (39). The structural morphologies of the deposited Mg and FeMn thin films are provided in figs. S2 and S3A, and the energy-dispersive x-ray spectroscopy (EDS) results show that the composition of Mn is  $\sim 32$  wt % in sputtered FeMn thin films (fig. S3A). The comparison of electrochemical characteristics of Fe and FeMn (fig. S3, B and C) suggests that the FeMn thin film holds a smaller charge transfer resistance, a more negative corrosion potential, and a larger corrosion current than those of Fe films, indicating a faster corrosion rate (estimated to be  $\sim 2.5$  times faster than that of the pure Fe film based on the corrosion current).

To topographically guide axonal outgrowth of nerve tissues, electrospun PCL nanofibers (thickness,  $\sim 30\ \mu\text{m}$ ) are coated on the metallic thin-film electrodes on the conduit (Fig. 1D). Figure 1E highlights the morphologies of DRG neurons cultured on PCL fibers (day 7), which exhibits extensive axonal sprouting and a highly aligned feature. The conduit materials and metallic thin films are fabricated in a planar format, and the subsequent rolling of the multilayer structure yields a three-dimensional (3D) miniaturized and electroactive conduit device, as shown in Fig. 1 (C and G).

The electrical performance of the Mg-FeMn galvanic cell is evaluated both *in vivo* and *in vitro*. Figure 1H presents the operating voltages of the electroactive conduit measured in an SD rat, 1, 2, and 3 days after implantation (the measurement setup is provided in fig. S4). With body fluids as the electrolyte, an average output open circuit voltage (OCV) of 0.984 V can be sustained after day 1, followed by 0.450 V on day 2, and then 0.068 V on day 3. The decreased voltage results from the gradual degradation of Mg metallic electrodes, indicating an electroactive life span of around 2 to 3 days *in vivo*. The anodic reaction proceeds with metal dissolution ( $\text{Mg} \leftrightarrow \text{Mg}^{2+} + 2\text{e}^-$ ), while the cathodic reaction involves either reduction of dissolved oxygen ( $\text{O}_2 + 2\text{H}_2\text{O} + 4\text{e}^- \leftrightarrow 4\text{OH}^-$ ) or hydrogen evolution ( $2\text{H}^+ + 2\text{e}^- \leftrightarrow \text{H}_2$ ) (32, 40). On the basis of the measured voltages, electric field distributions around the conduit device are simulated via finite element analysis, with the result on day 1 in Fig. 1I and more results in fig. S5. The generated electric field is predominantly distributed along the conduit in the range of  $\sim 20$  to 250 mV/mm, which is in accordance with the effective dc electric field intensity to enhance DRG neurite outgrowth, neurotrophic factors released by Schwann cells, and PC12 cell differentiation previously reported (4, 22–24). The electroactive galvanic cells are expected to stimulate surrounding nerve tissues that can be considered as a high impedance load (41) and promote regeneration and functional recovery. The *in vitro* discharge behaviors of Mg-FeMn galvanic cells are investigated in culture media with varied current densities and external loads (fig. S6). Decreased current densities and increased external resistances result in higher voltages. The OCV is measured to be  $\sim 1.0$  V in culture media, similar to the *in vivo* operational voltage on day 1. The *in vivo* operational time frame is longer than that obtained during *in vitro* tests, which is likely attributed to the difference in

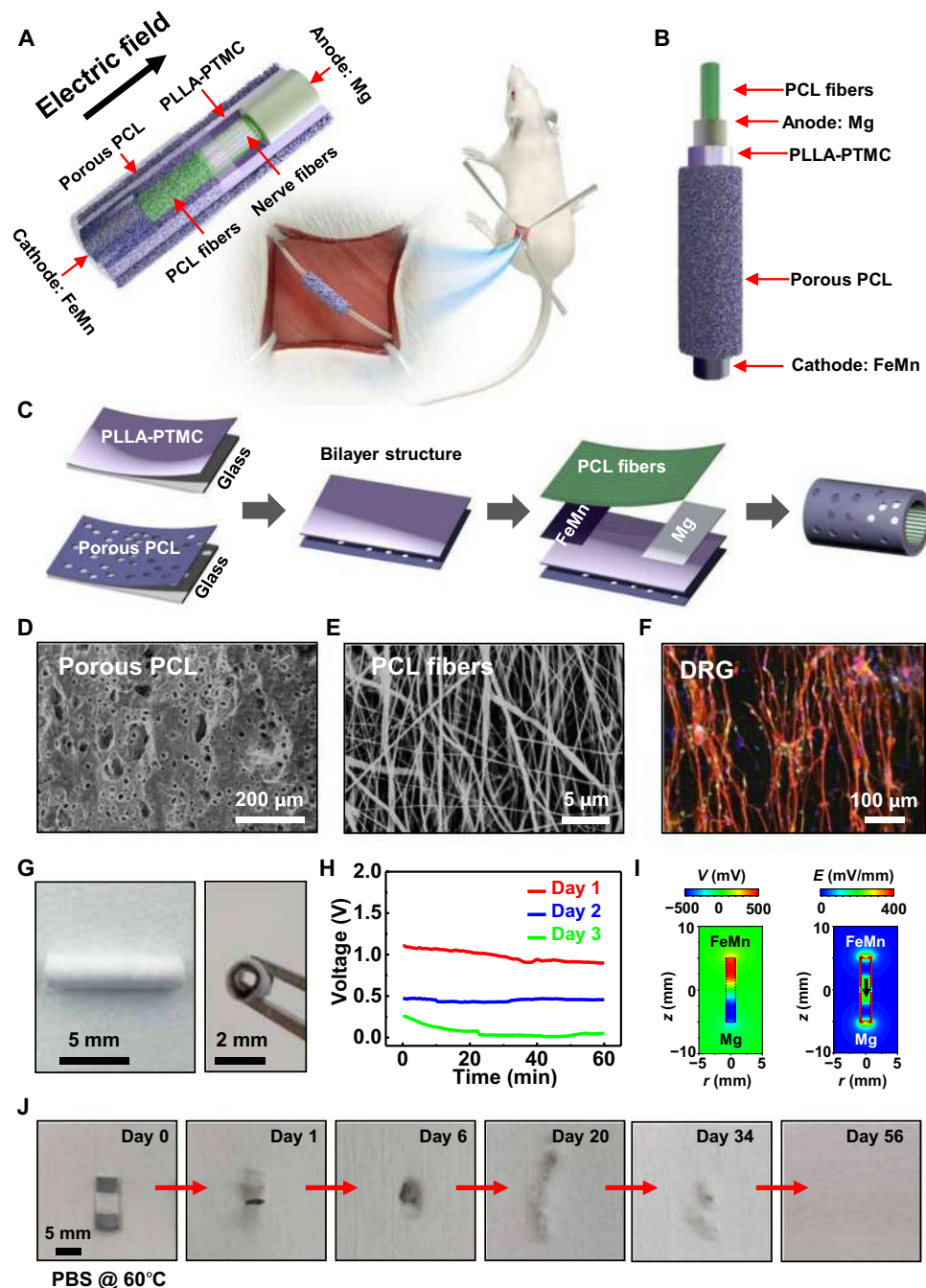


**Fig. 1. A biodegradable, self-electrified, and miniaturized conduit device for neuroregenerative medicine.** (A) Schematic illustration of the device for sciatic nerve regeneration. The device is composed of porous PCL (~350  $\mu\text{m}$ ,  $4.7 \times 10$  mm), PLLA-PTMC (~300  $\mu\text{m}$ ,  $4.7 \times 10$  mm), a Mg-FeMn galvanic cell (Mg ~3.5  $\mu\text{m}$ ,  $4.7 \times 3$  mm; FeMn ~1.5  $\mu\text{m}$ ,  $4.7 \times 3$  mm), and electrospun PCL fibers (~30  $\mu\text{m}$ ,  $4.7 \times 10$  mm). (B) Schematic exploded illustration of the device. (C) Fabrication process of the device. (D) SEM image of porous PCL. (E) SEM image of electrospun directional PCL fibers. (F) Confocal image of the guided neurite outgrowth of DRG neurons cultured on directional PCL fibers (day 7). Immunohistochemical staining: axons ( $\beta$ -tubulin, red), Schwann cells (S100, green), and nuclei (DAPI, blue). (G) Image of the electroactive device: front view (left) and side view (right). (H) In vivo measured OCV of an implanted device. (I) Finite element analysis of voltage (left) and electric field (right) distribution around the device on day 1 postoperatively. (J) Images collected at various stages of the accelerated dissolution of the device (planar state) in PBS (pH 7.4, 60°C). Photo credit: Liu Wang, Tsinghua University.

the electrolyte environments. There could be less amount of fluids in the in vivo environment, and the presence of proteins could potentially deposit on the electrode surface and limit the contact of body fluids to a certain extent, resulting in decreased dissolution

rates and longer lifetime of Mg-FeMn galvanic cells. Moreover, the lifetime of biodegradable galvanic cells could be extended by increasing the thickness of electrodes or adopting thicker encapsulation layers on the electrode surface.

To assess the degradation behavior of the miniaturized and self-powered conduit, the accelerated hydrolysis is observed in phosphate-buffered saline (PBS) solutions (pH 7.4, 60°C) at various stages (Fig. 1J). The results show that thin-film Mg electrodes disappear within 1 day, followed by complete dissolution of FeMn thin films after ~34 days, while polymeric conduit materials completely degrade after ~56 days.

### In vitro cell growth behavior with galvanic cells

To investigate the biocompatibility of the electrode materials of Mg-FeMn galvanic cells, PC12 and Schwann cells are cocultured with metallic thin films (Mg and FeMn) in culture media with experimental setup given in fig. S7. The results are shown in figs. S8 and S9. There is no significant difference of cell viability between the E-active group and the control group, indicating excellent biocompatibility. Growth behaviors of DRGs and Schwann cells are then investigated in vitro to evaluate the effects of the electric field provided by Mg-FeMn galvanic cells on nerve regeneration, with the same experimental setup given in fig. S7. Studies are performed with the control (no metallic films) and E-active (Mg-FeMn galvanic cells) groups, as well as the Mg (only Mg films) and FeMn groups (only FeMn films) to reveal the possible influence of individual metallic electrodes. The immunofluorescent images of DRG neurons after 7 days of culturing appear in Fig. 2A and fig. S10 (A and B). A greatly enhanced axonal outgrowth of DRGs is observed, with some neurites parallel to the electric field of Mg-FeMn galvanic cells. On the contrary, much shorter neurites of DRGs are observed in the control group (no electric field), and similar growth patterns are detected in both the Mg and FeMn groups (fig. S10, A and B). Quantitative analysis of the average neurite length of DRG neurons is summarized in fig. S10C. The results suggest that the average neurite length of DRGs is significantly longer in the E-active group than in the other groups ( $P < 0.01$ ), indicating that the electric field provided by Mg-FeMn galvanic cells plays an important role in promoting neurite extension. These results further support the biocompatibility of the electrode materials of Mg-FeMn galvanic cells. As the modulation of the electric field on neuronal growth is closely associated with the cellular calcium ( $\text{Ca}^{2+}$ ) signaling (42), the excitability of DRG neurons in both the E-active and control groups is further evaluated by monitoring spontaneous intracellular calcium signals in the cell soma (movies S1 and S2). Time-series fluorescent images of spontaneous intracellular calcium waves and quantitative analysis of the fluorescence intensities over time in the E-active group are illustrated in Fig. 2B. To quantify the observed calcium activity, the firing number and amplitude of calcium waves of individual neurons (cell number: 57 in the control group and 80 in the E-active group) within 250 s are analyzed and the results are given in Fig. 2C. The quantitative analysis indicates that the presence of the galvanic cell promotes more and stronger calcium waves compared to that in the control group, suggesting an enhanced calcium activity, which could activate effector proteins and elevate the level of neuronal cyclic adenosine monophosphate (cAMP) to provoke neurite outgrowth (42, 43). Moreover, Schwann cells respond to the electric field with faster proliferation, as compared with the control, Mg, and FeMn groups (Fig. 3A and fig. S11, A and B). Quantitative analysis of the number of Schwann cells (in the area of  $500 \mu\text{m} \times 500 \mu\text{m}$ ) reveals that the presence of galvanic cells significantly promotes cell proliferation compared to the other groups ( $P < 0.01$ ) (fig. S11C). The level of four neurotrophic factors, including nerve growth factor (NGF), brain-derived neuro-

trophic factor (BDNF), ciliary neurotrophic factor (CNTF), and vascular endothelial growth factor (VEGF), in supernatants of Schwann cells is measured by enzyme-linked immunosorbent assay (ELISA), and the results appear in Fig. 3B, fig. S11D, and table S1. The results suggest that the production of the four neurotrophic factors is boosted in the E-active, Mg, and FeMn groups relative to the control group ( $P < 0.01$ ; Fig. 3B and fig. S11D). The concentrations of CNTF, NGF, and VEGF in the E-active group are significantly higher than those in the Mg and FeMn groups ( $P < 0.01$ ; fig. S11D), probably due to the greatly enhanced proliferation of Schwann cells under the electric field. The concentration of BDNF in the E-active group is enhanced compared to that of the FeMn group ( $P < 0.05$ ), while no obvious difference is observed relative to the Mg group (fig. S11D). The enhanced expression of neurotrophic factors under the presence of electric field is consistent with the previous reports (44, 45). In all, the in vitro results indicate that Mg-FeMn galvanic cells are biocompatible and promote axonal outgrowth, calcium activities, Schwann cell proliferation, and neurotrophic factors that are all beneficial for nerve regeneration.

### In vivo nerve tissue regeneration with biodegradable and self-electrified conduit devices

Nerve grafts of the E-active (electroactive conduit), autograft, and hollow (conduit without metallic films) groups are implanted to bridge a 10-mm transected sciatic nerve gap in SD rats to evaluate the efficacy of electroactive conduits on nerve regeneration, as shown in Fig. 4A. The detailed process of the surgical procedure is given in movie S3. Studies are also performed with Mg (conduit with only Mg films) and FeMn (conduit with only FeMn films) groups to assess the potential influence of individual metallic electrodes. It is noted that the electrospun PCL layer is also present on the inner surface of the conduits of the hollow, Mg, and FeMn groups, and the only difference between the hollow and E-active groups is the absence of galvanic cells. MRI is frequently involved in clinical diagnosis, and conductive components of biomedical implants could interact with electromagnetic fields, causing device heating and image distortion. The MRI images with and without implanted electroactive devices appear in Fig. 4B. Sciatic nerves and the location of the electroactive conduit can be clearly identified, where the white contrast at the transected nerves indicates the presence of fluids inside the conduit probably due to potential inflammation and swelling induced by surgery. The absence of image distortion suggests low magnetic susceptibility of Mg and FeMn thin films in the electroactive device. Micro-computed tomography (micro-CT) is an alternative technique to complement evaluation of nerve regeneration and track the degradation process of metallic thin films of implanted devices. An example of micro-CT image is given in Fig. 4C, where the location of the implanted conduit device (dark tube-like area) and the FeMn thin film (white contrast) can be captured. Time-series micro-CT images taken at different stages of the E-active group appear in fig. S12, and results suggest that tissues have grown into the conduit area and FeMn thin films remain after 12 days of implantation. As micro-CT images cannot differentiate the types of tissues in the conduit, immunohistochemical studies of the cross-sectional nerve tissues are used to evaluate the regrowth of nerve tissues. It is noted that the immunofluorescent staining of the transverse sections is often adopted for evaluation especially at the later stage of nerve regeneration (10, 21), as it is important to investigate the degree of nerve fiber myelination and axonal maturity through

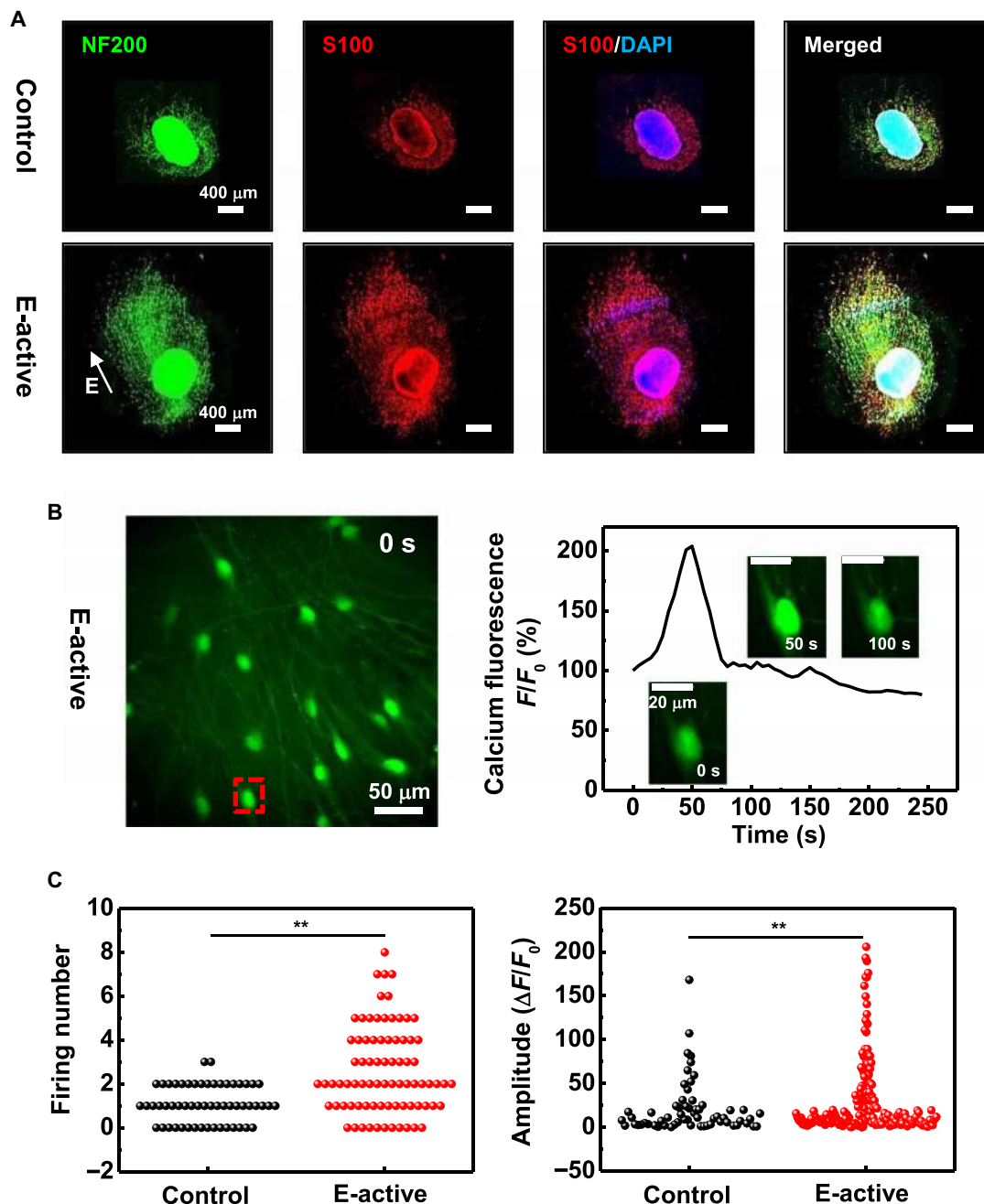


**Fig. 2. In vitro DRG neuron growth behavior with Mg-FeMn galvanic cells.** (A) Confocal microscope images of DRG neurons cultured with galvanic cells (the E-active group) and no metallic films (the control group) on day 7. The white arrow indicates the direction of the electric field. Immunohistochemical staining: axons (NF200, green), Schwann cells (S100, red), and nuclei (DAPI, blue). (B) Calcium dynamics within the DRG neurons in the E-active group (calcium, green). Left: Photo of DRG neurons after calcium dye loading. Right: Example showing the time-series imaging of calcium dynamics of the neuron in the red dashed box from the left. The cell soma was chosen as the region of interest for drawing the trace. Three images at designated time show the fluorescent intensity change. (C) Quantification of the number (left) and amplitude (right) of calcium waves within 250 s of individual neuron of the E-active and control groups (cell number: 57 in the control group; 80 in the E-active group). GraphPad Prism (version 6.0) was used for the statistical analysis, followed by unpaired *t* test (\*\* $P < 0.01$ ).

the cross-sectional sections of regenerated nerves. Together with a series of systematic evaluations of functional recovery through electrophysiological evaluation, gastrocnemius muscle assessment, and walking track analysis at 12 weeks after implantation, the therapeutic effects of the electroactive devices will be critically assessed.

To obtain consistent results, the transverse sections of regenerated tissues are investigated at 3, 9, and 12 weeks after implantation, and the locations of different sections are summarized in fig. S13. At each time point, the same locations of transverse section are obtained to compare among different groups, and representative results are

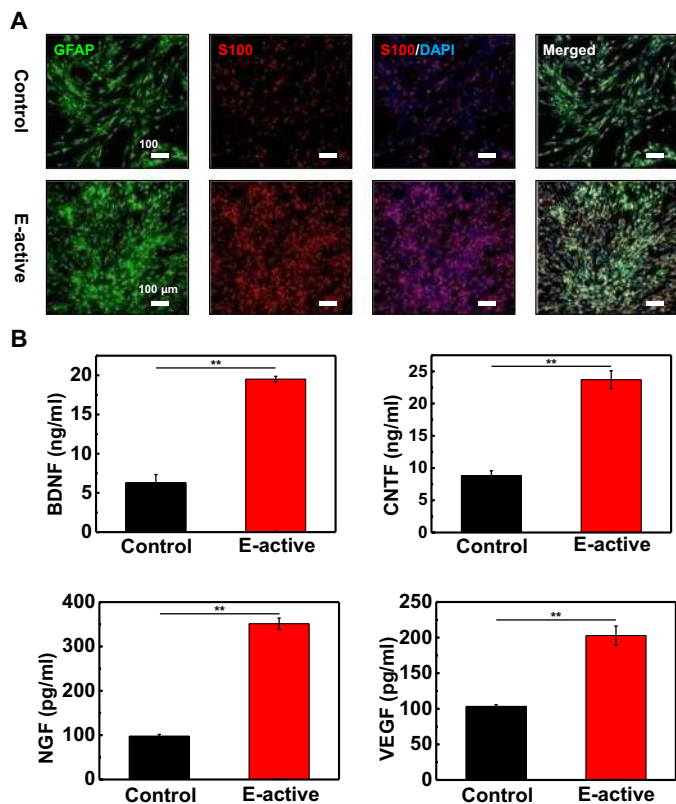


**Fig. 3. In vitro Schwann cell growth behavior with Mg-FeMn galvanic cells.** (A) Confocal microscope images of Schwann cells of the E-active and control groups on day 3. (B) ELISA of BDNF, CNTF, NGF, and VEGF production in Schwann cells of the E-active and control groups. Data are mean  $\pm$  SD. Immunohistochemical staining: Schwann cells [glial fibrillary acidic protein (GFAP), green], Schwann cells (S100, red), and nuclei (DAPI, blue).  $n = 3$  independent experiments per group. The SPSS software package (version 23.0) was used for the statistical analysis, followed by one-way ANOVA (\*\* $P < 0.01$ ).

given. To evaluate the effects of the electroactive conduit devices on nerve regeneration at the early stage, immunofluorescent images of transverse sections at the middle of the nerve segment (one-half section) at 3 weeks after implantation are given in Fig. 4D and fig. S14. Figure S15 summarizes the full cross-sectional view of regenerated nerve tissues of all the groups. The area of regenerated axons and Schwann cells in the E-active group is much larger than that in the hollow group (Fig. 4D and fig. S15), indicating a much higher nerve regeneration rate facilitated by the presence of galvanic cells. The axonal density in the E-active group is higher relative to the Mg and FeMn groups (Fig. 4D and fig. S14), indicating the positive effects of electric field introduced by the galvanic cells. It is noted that the area of regenerated nerve tissues in the autograft group appears to be the greatest compared to the other groups, which is expected due to the presence of proper axonal and Schwann cells immediately after surgery. Hematoxylin and eosin (H&E) staining images appear in fig. S16, indicating no significant inflammations. As the formation of new blood vessels is closely associated with nerve regeneration at the early stage, the immunofluorescent staining of endothelial cells (ECs) of the transverse sections is also performed (fig. S17), and the density of ECs exhibits a consistent trend with that of the regenerated nerve tissues.

The immunofluorescent images of transverse sections of nerve tissues (two-third section and distal section of the nerve segment) at 9 weeks after implantation appear in figs. S18 to S20, and H&E staining images are given in fig. S21. These results represent the middle stage of nerve regeneration, and regenerated nerve tissues are found to regrow beyond two-thirds of transected gaps in all groups. Comparable with the autograft group, the E-active group demonstrates larger area of regenerated nerve tissue at the two-third sections compared to that of the hollow, Mg, and FeMn groups. These results are virtually consistent with the trend observed at 3 weeks after implantation, indicating the improved therapeutic effects of electroactive devices at both early stage and middle stage of nerve regeneration. It is noted that the observed tissues at the distal sections are likely the residual transected nerve stumps, as the cross-sectional area is larger than that at the two-third sections in all the treated groups except the autograft one. Nevertheless, the H&E results (fig. S21) at both the two-third and distal sections indicate no significant inflammations.

The evaluation of sciatic nerve regeneration at the later stage is performed through immunohistochemical staining and transmission electron microscopy (TEM) techniques at 12 weeks postoperatively. The immunofluorescent images of transverse sections at the middle of regenerated nerve segment (one-half section) are given in Fig. 5A and fig. S22A. The TEM images of the regenerated nerves further reveal more details of the degree of nerve fiber myelination and axonal maturity (Fig. 5B and fig. S22B). The quantitative analysis of g-ratio (area-based), the diameters of myelinated nerve fibers, and the thickness of myelin sheath based on TEM images is summarized in Fig. 5 (C and D) and fig. S22 (C to E). The average g-ratio is an indicator of the degree of axonal myelination, and the results suggest that the g-ratio is similar among the E-active, autograft, and Mg groups, and a lower degree of myelination is observed in the hollow and FeMn groups ( $P < 0.01$ ) (Fig. 5C and fig. S22C). The average diameters of myelinated nerve fibers in the E-active group are greater than those in the hollow, Mg, and FeMn groups ( $P < 0.01$ ) (Fig. 5D and fig. S22D), implying a greater axonal maturity. In addition, the average thickness of myelin sheath in the E-active group is similar to that in the Mg group, and it is greater relative to the hollow ( $P < 0.01$ ) and FeMn groups ( $P < 0.05$ ) (fig. S22E). The greatest myelinated fiber diameter and myelin sheath thickness are found in the autograft group ( $P < 0.01$ ), which is expected because of the cellular scaffold and the presence of bioactive cues such as Schwann cell basal lamina and growth factors. These results suggest that the electric field offered by the electroactive conduit devices endow positive effects in remyelination of the regenerated nerves.

### Functional recovery with biodegradable and self-electrified conduit devices

As function recovery is the key assessment of peripheral nerve regeneration, studies have been performed through electrophysiological evaluation, gastrocnemius muscle assessment, and walking track analysis at 12 weeks after implantation. Electrophysiological tests are used to evaluate nerve conduction recovery. The compound motor action potential (CMAP) is measured by recording the action potential of target gastrocnemius muscles after electrically stimulating the proximal sciatic nerve stumps at the injured side. The representative CMAP curves appear in Fig. 6A and fig. S23A. Although statistical analysis suggests no significant difference in CMAP latency

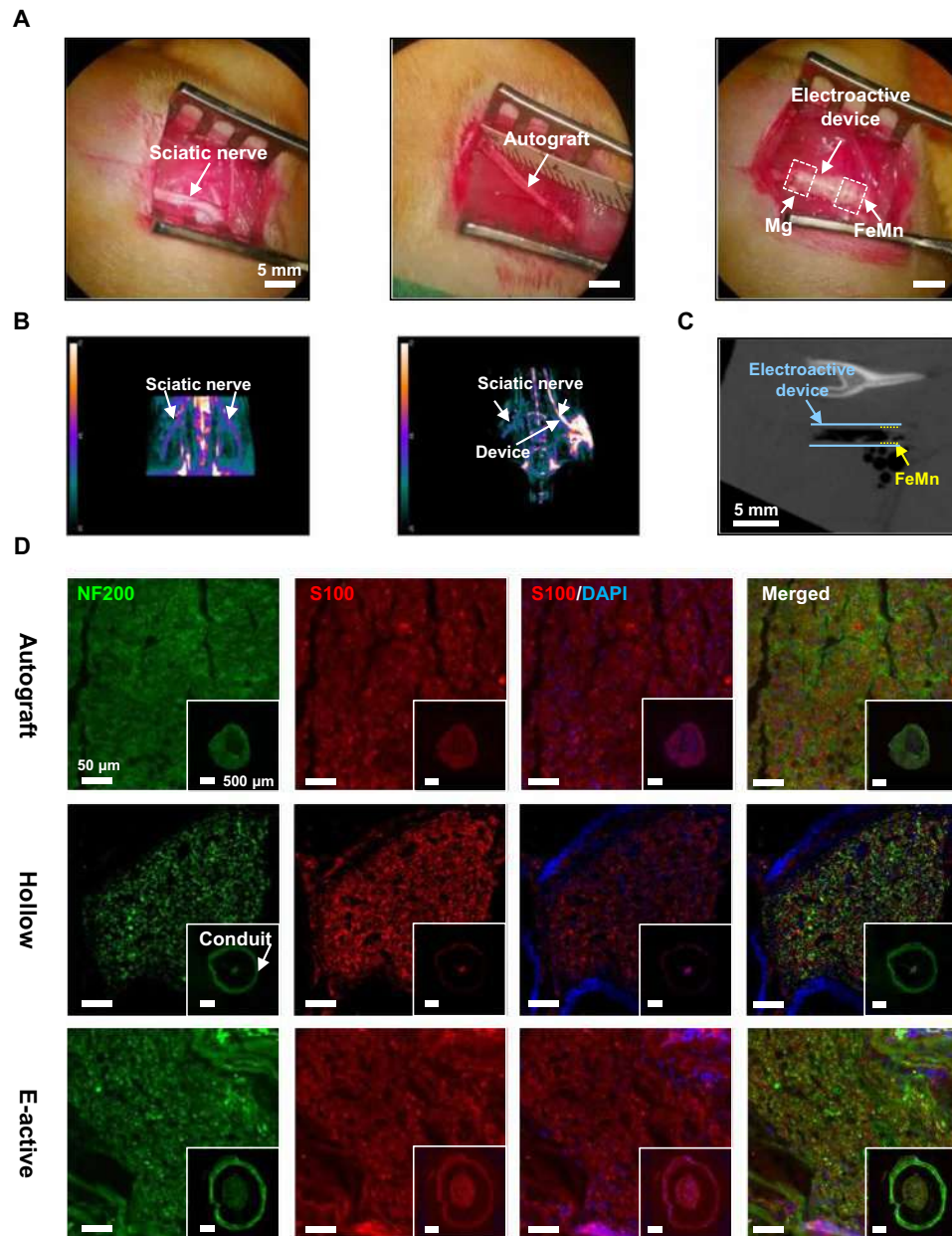


**Fig. 4. Sciatic nerve regeneration with biodegradable and electroactive conduit devices.** (A) Surgical images of the implantation of electroactive conduit devices at the sciatic nerves of SD rats. Left: Sciatic nerves. Middle: Implantation with an autograft. Right: Implantation with an electroactive conduit device. (B) MRI images of sciatic nerves (left, no implantation) and an electroactive conduit device (right, day 7 after implantation). The white contrast at the implantation site results from swelling after surgery. (C) Micro-CT image of an electroactive conduit device (day 1 postoperatively). The black tube-like region indicates the location of the electroactive device (marked with blue lines). The white contrast on the electroactive device indicates FeMn thin films (marked with yellow dotted lines). (D) Immunofluorescent images of the transverse sections of regenerated tissues at the middle of the nerve segment at 3 weeks after implantation of the autograft, hollow, and E-active groups. The immunofluorescent images at lower magnification in the insets give the full view of regenerated tissues. Immunohistochemical staining: axons (NF200, green), Schwann cells (S100, red), and nuclei (DAPI, blue). Photo credit: Liu Wang, Tsinghua University.

for all the groups (Fig. 6E and fig. S23C), the CMAP amplitude of the E-active group is improved relative to the hollow (Fig. 6D) and Mg groups ( $P < 0.05$ ) (fig. S23B), suggesting that much more innervated muscle fibers and regenerated motor units are achieved by using electroactive devices. It is noted that the autograft group demonstrates higher CMAP amplitude than all the other groups (Fig. 6D and fig. S23B).

Sciatic nerve transection results in the loss of innervation in gastrocnemius muscles that often leads to atrophy if reinnervation cannot be achieved properly after motor nerve regeneration. To investigate the degree of muscle atrophy at the injured hindlimb, which is an important index of functional recovery, analysis of ultrasound images, muscle wet weight ratios, and Masson trichrome staining of the transverse gastrocnemius muscle sections at 12 weeks after

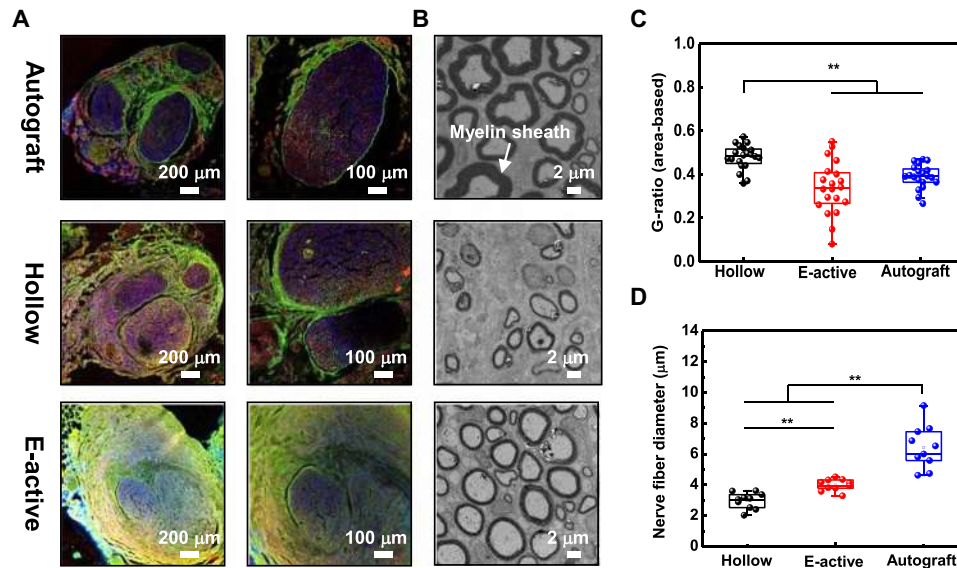


**Fig. 5. Evaluations of regenerated nerve fibers at 12 weeks after implantation of the autograft, hollow, and E-active groups.** (A) Immunofluorescent images of the transverse section at the middle of the nerve segment (one-half section). Immunohistochemical staining: axons (NF200, green), Schwann cells (S100, red), and nuclei (DAPI, blue). (B) TEM images of the transverse sections (one-half section) of regenerated sciatic nerves. (C) Average area-based g-ratio. (D) Average diameters of myelinated axons.  $n = 5$  independent animals per group. The SPSS software package (version 23.0) was used for the statistical analysis, followed by one-way ANOVA (\*\* $P < 0.01$ ).

implantation are performed. Ultrasound imaging is a noninvasive technique to examine the elasticity of gastrocnemius muscles. Quantitative analysis of ultrasound results (Fig. 6F and fig. S24) reveals that the muscle elasticity in the E-active group is slightly higher than that in the autograft group ( $P < 0.05$ ), and it is lower compared to the results in the hollow, Mg, and FeMn groups ( $P < 0.01$ ), indicating improved muscle reinnervation and the recovery of muscle atrophy with electroactive devices. Representative gross images of gastrocnemius muscles isolated from both the injured and contralateral (unoperated) hindlimbs (Fig. 6B and fig. S25A) suggest apparent atrophy in the hollow, Mg, and FeMn groups compared to that of the E-active and autograft groups. To quantitatively evaluate muscle atrophy, the gastrocnemius muscles on the operated legs are compared to the healthy ones to calculate the muscle wet weight ratio, and the results appear in Fig. 6G and fig. S25B. The results indicate that the wet weight ratio of the E-active and autograft groups is close ( $P < 0.05$ ), and it is significantly higher than that of the hollow, Mg, and FeMn groups ( $P < 0.01$ ), consistent with the ultrasound results. The Masson's trichrome staining images of the transverse sections of gastrocnemius muscles from the injured limbs are given in Fig. 6C and fig. S26A. Significantly less collagenous deposits and larger average cross-sectional muscle fiber area are found in the E-active and autograft groups, suggesting a better muscle reinnervation. Statistical analysis of the cross-sectional area of muscle fibers (Fig. 6H and fig. S26B) shows that the muscle fiber area in the E-active group is slightly lower than that in the autograft group ( $P < 0.01$ ), and it is greater than that in the hollow, Mg, and FeMn groups ( $P < 0.01$ ). These results further suggest the positive therapeutic effects in muscle reinnervation promoted by the electrical field of electroactive devices.

To assess the recovery of motor functions along nerve regeneration, the CatWalk system is used to evaluate walking track every 2 weeks postoperatively. Figure 7A and fig. S27A illustrate the 3D plantar pressure distributions of the contralateral (unoperated)

hindlimb and right hindlimb (injured side) obtained at 12 weeks after implantation. The  $y$  axis of the 3D plantar pressure distribution displays the relative intensity of the scattered light brightness in arbitrary units, which implies the corresponding relative pressure of the plantar. The results indicate that both the print area and the plantar pressure of the E-active group are comparable to those of the autograft group. The statistical results of sciatic function index (SFI), a measure of sciatic nerve function, are calculated by four different parameters of footprints, and the results appear in Fig. 7B and fig. S27B. SFI values close to 0 suggest normal motor function, while SFI values close to  $-100$  indicate severe dysfunction. In all cases, SFI values demonstrate a decreasing trend at the initial 4 weeks after implantation, which indicates the impaired motor function induced by sciatic nerve transection, followed by an increasing trend in a time-dependent manner afterward, suggesting the gradual recovery of motor function due to nerve regeneration. Although there is no significant difference of SFI values in all groups at 2 and 4 weeks, the E-active group demonstrates greatly higher SFI values after 4 weeks compared to the hollow, Mg, and FeMn groups ( $P < 0.01$ ) (Fig. 7B and fig. S27B). The SFI values at 12 weeks after implantation of the hollow, E-active, and autograft groups are  $-69.82 \pm 3.06$ ,  $-41.51 \pm 5.47$ , and  $-37.71 \pm 3.13$ , respectively. There is no statistical difference of the SFI values between the E-active and autograft groups at 10 and 12 weeks after implantation (Fig. 7B), indicating excellent motor function recovery with the electrical cue provided by the electroactive conduit. The walking track of SD rats at 12 weeks after implantation of the hollow, E-active, and autograft groups is given in movie S4 to demonstrate the enhanced functional recovery in the E-active and autograft groups.

These combined results of immunohistochemistry, electrophysiology, muscle atrophy evaluation, and functional assessment prove the therapeutic efficacy of the biodegradable and self-electrified conduits, with equivalent outcomes of the improved axonal remyelination and motor function recovery as compared to the autograft

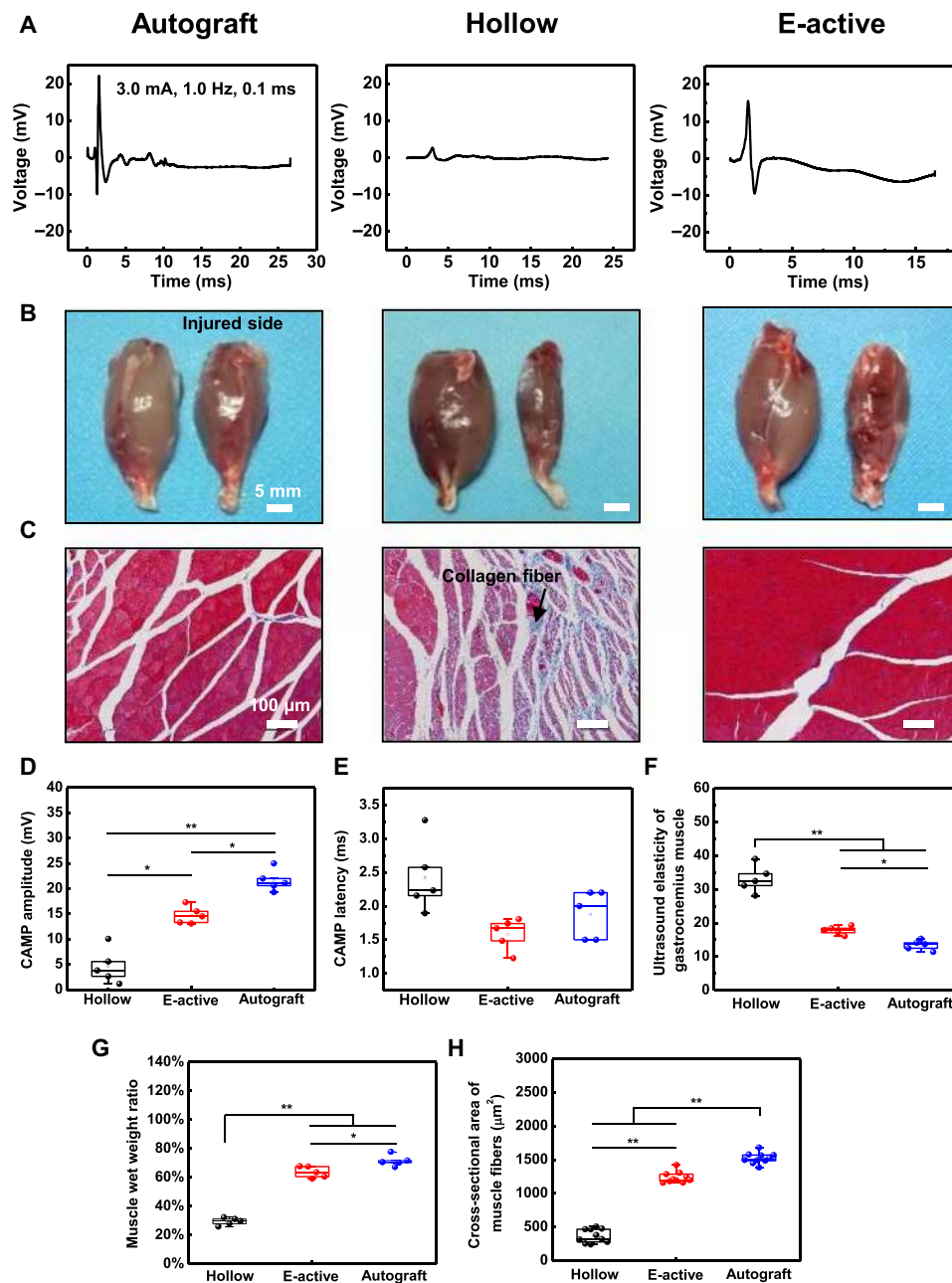


**Fig. 6. Evaluation of gastrocnemius muscles at 12 weeks after implantation of the autograft, hollow, and E-active groups.** (A) Representative CMAP at the injured side. Electrical stimulation (3.0 mA, 1 Hz, 0.1 ms) is applied at the proximal and distal nerve stumps. (B) Gross images of the isolated gastrocnemius muscles of the contra-lateral (unoperated, left) and injured side (right). (C) Masson's trichrome staining images of the transverse sections of muscles from the injured limb. (D) Statistical analysis of CMAP amplitude at the injured side. (E) Statistical analysis of CMAP latency at the injured side. (F) Statistical analysis of the ultrasound elasticity of gastrocnemius muscles from the injured limb. (G) Statistical analysis of the wet weight ratio of the gastrocnemius muscles from the injured limb. (H) Statistical analysis of the area of muscle fibers from the injured limb quantified from Masson's trichrome staining images.  $n = 5$  independent animals per group. The SPSS software package (version 23.0) was used for the statistical analysis, followed by ANOVA ( $*P < 0.05$  and  $**P < 0.01$ ). Photo credit: Changfeng Lu, Chinese PLA General Hospital.

treatment. The results of functional recovery (SFI) are comparable with the previous report, where transcutaneous low-frequency electrical stimulation (1 hour every 2 days for seven times) was applied through nondegradable conductive scaffolds (21). The enhanced therapeutic effects suggest that the presence of the electric field induced by the self-electrified conduit at the early stage of nerve re-

generation (first 2 to 3 days) could be crucial for motor function recovery, as it could assist faster axonal regrowth and reduce the total time of distal muscle denervation, improving functional recovery quality. It is noted that the previously reported electrical stimulation spans a variety of parameters, including low-frequency pulse ac stimulation (monophasic or biphasic) (20, 28) and dc electric

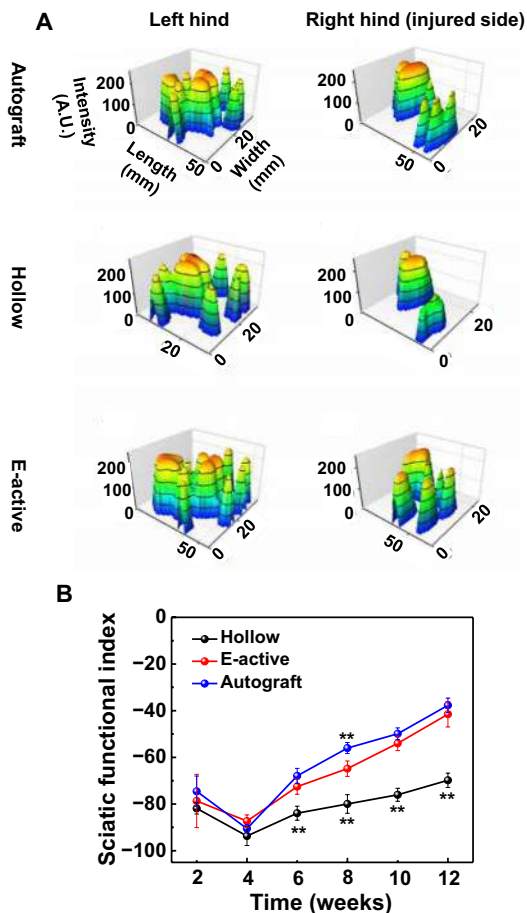


**Fig. 7. Evaluation of the motor functional recovery of the autograft, hollow, and E-active groups.** (A) 3D plantar pressure distribution of walking track of SD rats at 12 weeks after implantation. A.U., arbitrary units. (B) SFI values close to 0 suggest normal motor function, while SFI values close to  $-100$  indicate severe dysfunction. Data are mean  $\pm$  SD. For each group,  $n = 11$  for week 2;  $n = 8$  for weeks 4, 6, and 8; and  $n = 5$  for weeks 10 and 12. The SPSS software package (version 23.0) was used for the statistical analysis, followed by ANOVA (\*\* $P < 0.01$  versus E-active group).

field (19), with stimulation time ranging from a few hours to repeated short-term daily stimulation, and their beneficial effects at the early stage of nerve regeneration are believed to be associated with elevated cAMP and up-regulation of neurotrophic factors (45, 46). Faster elongation and directional growth of neurites have been observed under dc electric field, which could be mediated by cytoplasmic calcium and cAMP (47–49). Combined with the in vitro results in the current work, the beneficial effects of the dc electric field provided by the galvanic cell could be attributed to the stimulation of Schwann cell repopulation, up-regulation of neurosupportive growth factors, and enhanced calcium activity that could activate effector proteins and enhance cAMP levels promoting neuronal outgrowth (4, 24, 42). It is worth mentioning that although dc electrical stimulations could be of concern for conventional non-degradable electrical stimulators because of potential dissolution of electrodes, materials in the electroactive device are designed to be biocompatible and biodegradable and will not likely cause significant tissue toxicity.

In summary, we report a biodegradable, self-electrified, and miniaturized therapeutic conduit device coupling galvanic cells and nerve guidance conduit that can provide both structural guidance and self-sustained electrical stimulation beyond intraoperative window to promote peripheral nerve regeneration (10-mm nerve gap). The self-powered nature of the device avoids the dependence of external equipment for power delivery, ensuring operational convenience. The entire device is biocompatible and fully biodegradable in physiological solutions, eliminating a second surgery for device retraction. As the key electroactive component of the devices, the Mg-FeMn galvanic cell has been shown to prominently facilitate axonal outgrowth and calcium activity of DRG neurons and promote proliferation and neurotrophic factor production of Schwann cells. The biodegradable and electroactive device demonstrates efficacy in promoting sciatic nerve regeneration in rodents by enhancing the growth of nerve tissues and accelerating recovery of motor functions. Restored motor functions facilitated by the electroactive devices are comparable with that of autografts, which are often involved in clinical treatments, shedding light on potential novel non-pharmacological self-powered electronic medicine treating peripheral nerve injuries without additional surgical complications such as second surgeries and donor site morbidity.

Materials strategies and device schemes proposed in the current work establish essential baselines for biodegradable, self-powered, and miniaturized devices that can deliver postoperative electrical therapies inside the human body without requiring external sources. Future directions include optimization of the operational lifetimes and electric field intensity of the self-electrified device and development of alternative electrical signals with pulse modes. Incorporation of multifaceted cues will also be critical to further encourage nerve regrowth, such as biomimetic luminal fillers, biodegradable and conductive coating pathways, and neurotrophic factors. Combining the electroactive conduit with autografts that have excellent biological cues represents another possibility to further promote nerve regeneration, as clinical treatments have demonstrated positive effects by adding electrical cues with autologous nerve grafting. Moreover, as large-gap ( $>2$  to 3 cm) injury repair remains a great challenge using artificial conduits, assessment of nerve regeneration by the electroactive device with comparable size on large animal models is crucial. Collectively, the biodegradable and self-electrified conduit devices may potentially be applied to various target tissues and organs where electrical fields are necessary to intervene biological functions, enabling innovative approach to tackle the hurdles in regenerative medicine.

## MATERIALS AND METHODS

### Fabrication of biodegradable and electroactive therapeutic devices

PLLA-PTMC films (thickness,  $\sim 300$   $\mu\text{m}$ ; size,  $\sim 4.7$  mm  $\times$  10 mm) were achieved by dissolving PLLA-PTMC (60:40, viscosity of 2.2 mPa·s; Jinan Daigang Biomaterial Co. Ltd., China) into trichloromethane ( $\text{CHCl}_3$ ) (Beijing Tongguang Chemical Co. Ltd., China) with a weight-to-volume (w/v) ratio of 1:10, followed by drop-casting and curing for 12 hours at  $4^\circ\text{C}$  to avoid bubble formation. Concentrations of chemicals in the current work are all reported in a w/v ratio unless otherwise noted. Porous PCL films (thickness,  $\sim 350$   $\mu\text{m}$ ; size,  $\sim 4.7$  mm  $\times$  10 mm) were fabricated by mixing PCL (average molecular weight of  $\sim 80,000$ ; Beijing Dibaier Biotechnology Co. Ltd., China)

and sodium chloride (NaCl) with dimethylformamide (Sigma-Aldrich Inc., USA) at concentrations of 15% and 4% solutions at 45°C. The mixture was then casted on glass substrates, and the resulting films were soaked in distilled water to remove NaCl particles, allowing the formation of porous PCL films. A bilayer conduit material was prepared by laminating PLLA-PTMC to the porous PCL using a small amount of  $\text{CHCl}_3$  solution. Mg thin-film anodes (thickness,  $\sim 3.5 \mu\text{m}$ ; size,  $\sim 4.7 \text{ mm} \times 3 \text{ mm}$ ) were deposited on one side of the bilayer material through a shadow mask in a magnetron sputter (Beijing Zhongjingkeyi Co. Ltd., China) with a deposition speed of  $1.8 \text{ \AA s}^{-1}$  (280 V, 0.23 A) through patterned shadow masks. Similarly, FeMn alloy thin films (thickness,  $\sim 1.5 \mu\text{m}$ ; size,  $\sim 4.7 \text{ mm} \times 3 \text{ mm}$ ) used as the cathodes were fabricated on the other side of the conduit through magnetron sputtering, using a customized target made of FeMn alloy with 30 wt % Mn, with a deposition speed of  $1.1 \text{ \AA s}^{-1}$  (340 V, 0.25 A). The electrospinning solution used to fabricate directional PCL fibers was obtained by dissolving PCL particles into hexafluoroisopropanol (Shanghai Aladdin Biochemical Co. Ltd., China) with a w/v ratio of 1:14. The PCL solution was then electrostatically drawn from the tip of a 10-ml syringe onto the surface of the metallic thin-film electrodes at a mass flow rate of  $0.3 \text{ mm min}^{-1}$  by applying a high voltage of 15 kV between the electrode and a rotating collector (850 rpm) to achieve a layer of directional electrospun PCL fibers (thickness,  $\sim 30 \mu\text{m}$ ; size,  $\sim 4.7 \text{ mm} \times 10 \text{ mm}$ ). A 3D electroactive device was achieved by rolling up the planar multilayer structure on a needle (diameter, 1.5 mm), which determined the inner diameter of the device. Given the tackiness, a freshly prepared thin layer of electrospun PCL ( $\sim 20 \mu\text{m}$ ) was wrapped around the conduit to fix the shape.

### Evaluations of materials morphology, mechanical properties, and biodegradability

Material surface morphology was investigated by a field-emission scanning electron microscopy (SEM) system (Zeiss, Belin, Germany), and EDS technique was used to investigate the composition of sputtered thin films. Tensile tests were carried out using a universal testing machine (WDW3020, Kexin Co. Ltd., China) with a specimen size of  $10 \text{ mm} \times 0.35 \text{ mm} \times 50 \text{ mm}$  at a strain rate of  $0.002 \text{ s}^{-1}$ . The elastic modulus and tensile strength are calculated by the software (three measurements for each material), and the results are shown as mean  $\pm$  SD. The degradation experiments were performed by soaking the electroactive devices (in the planar state) in PBS (replaced every day) at 60°C using a water bath, and time-series images are taken by an optical microscope at various stages.

### Electrochemical measurements

For in vitro evaluation, Mg-FeMn galvanic cells were fabricated by sputtering metallic thin films (size,  $0.5 \text{ cm} \times 9 \text{ cm}$ ; thickness, Mg,  $3.5 \mu\text{m}$ , and FeMn,  $1.5 \mu\text{m}$ ) on polyethylene terephthalate substrates with encapsulation of a layer of PLLA-PTMC ( $\sim 50 \mu\text{m}$ ). The discharge behavior of Mg-FeMn galvanic cells (electrode surface area,  $1 \text{ cm}^2$ ) with culture media (RPMI 1640 medium, Thermo Fisher Scientific Co. Ltd., Hampton, NH, USA) as the electrolyte was investigated with various current densities and external loads using a battery tester (Neware Electronic Corporation, Shenzhen, China). Three measurements per discharge condition were performed, and representative curves were given as the results. The OCV of galvanic cells was measured by a potentiostat (Interface 1000E, Gamry, USA). For in vivo evaluation, electroactive devices were fabricated following the aforementioned process. Mg and FeMn alloy thin-film electrodes

were connected to copper wires through a biodegradable conductive paste made of PLLA-PTMC and Mo particles. The connection was encapsulated by 3140 adhesive (Dow Corning Corp., MI, USA) and poly(dimethyl siloxane) to ensure durable electrical contact. The OCV was measured by a potentiostat for 1 hour every day until it drops to zero. Three independent experiments were performed ( $n = 3$ ), and representative curves were given as the results. The galvanodynamic polarization curves and electrochemical impedance of Fe and FeMn alloy were measured by a potentiostat (Interface 1000E, Gamry, USA) in PBS using a three-electrode configuration with Fe or FeMn alloy as the working electrode, Ag/AgCl as the reference electrode, and platinum as the counter electrode. Three measurements were performed for each sample. Galvanodynamic polarization curves were measured at a scanning rate of  $0.2 \text{ mV s}^{-1}$  and a varying potential of  $\pm 0.25 \text{ V}$ . Electrochemical impedance spectroscopy measurements were performed from 1 Hz to 1 MHz with an amplitude of 5 mV and 0 V bias from the OCV.

### Simulation of the electric field

The simulations of voltage and electric field distribution around the electroactive conduit were performed by finite element methods in COMSOL Multiphysics using the ac/dc module. The conduit was defined as a hollow cylinder, with an inner diameter of 1.5 mm, an outer diameter of 2 mm, and a height of 10 mm. Tissue around the conduit was modeled as a cylinder with a diameter of 50 mm and a height of 40 mm. The conduit materials were assumed as electrical-insulating with a relative permittivity of 2.75 (50). PBS solution was used as the electrical equivalent to tissue around the conduit with a conductivity of  $1.5 \text{ S m}^{-1}$  (51–53) and a relative permittivity of 80 (52, 53). The galvanic cells (FeMn cathodes and Mg anodes, 3 mm in height each) were defined to have constant voltages, the values of which were acquired from in vivo experiments. The cross-sectional plane of calculated voltages and electric fields was plotted.

### Cytotoxicity tests

Cytotoxicity tests were performed by coculturing galvanic cells (Mg and FeMn thin films with a distance of  $\sim 3 \text{ mm}$ ) with Schwann cells and PC12 cell lines. Three independent experiments were conducted for each type of cells ( $n = 3$ ). PC12 cell lines (Tiandz Inc., China) were cultured in 1640 medium supplemented with 10% horse serum and 5% fetal bovine serum (FBS) for 7 days. Schwann cells were harvested and purified as described previously (54, 55). Briefly, the sciatic nerves of 3-day-old SD rats were enzymatically dissociated with 1 ml of 0.2% collagenase. Next, the mixtures were stirred at 37°C for 10 min, centrifuged, and resuspended in Dulbecco's modified Eagle's medium and nutrient mixture F-12 (DMEM/F12) supplemented with 10% (v/v) FBS NB4 (Sigma-Aldrich) after trituration for 5 min. The purified Schwann cells were cultured with nutrient mixture F-12 (DMEM/F12) supplemented with 10% FBS,  $2 \mu\text{M}$  GlutaMAX, 2% double antibody, epidermal growth factor ( $10 \text{ ng ml}^{-1}$ ), and  $2 \mu\text{M}$  forskolin for 7 days. After culturing, the medium was removed and the cells were washed three times and then stained with calcein-AM/ethidium homodimer-1 (Thermo Fisher Scientific Co. Ltd., Hampton, NH). The fluorescent images were obtained with fluorescent microscopy (Ni-U, Nikon Co., Japan).

### In vitro cell growth behavior and immunohistochemical and ELISA analysis

DRG neurons were isolated from postnatal day 1 rat pups following a previously described procedure (56). They were then cocultured

with deposited metallic films (thickness, Mg, 3.5  $\mu\text{m}$ , and FeMn, 1.5  $\mu\text{m}$ , with a distance of  $\sim 3$  cm) in different experimental groups incubated in a constant temperature incubator (5%  $\text{CO}_2$ , 37°C) for 7 days. The investigation was performed with four groups: control (no metallic films), E-active (Mg-FeMn galvanic cells), Mg (only Mg films on both ends), and FeMn (only FeMn films on both ends). Three independent experiments were conducted for each group ( $n = 3$ ). The culture medium is DMEM/F12 (Gibco, USA) with B-27 (2%; Gibco, USA) and penicillin-streptomycin (1%). The solutions were changed every 2 days. After culturing, DRGs were fixed in paraformaldehyde (4%) for 30 min, permeabilized with Triton X-100 (0.3%) for 5 min, and incubated with normal goat serum (10%; Solarbio, China) for 30 min at room temperature. Next, DRGs were incubated with mouse anti-NF200 antibodies (Sigma-Aldrich, USA) and rabbit anti-S100 antibodies (Sigma-Aldrich, USA) at 4°C overnight and then secondary antibodies with the goat anti-rabbit antibodies (IgG H+L, Alexa Fluor 594, Abcam, USA) and goat anti-mouse antibodies (IgG H+L, Alexa Fluor 488, Abcam, USA) for 1 hour in the dark at room temperature. After washing three times with PBS, the samples were stained with 4',6-diamidino-2-phenylindole (DAPI; 1:200) for 5 min, washed three times with PBS, and observed via confocal laser scanning microscopy (LSM 780, Zeiss, Oberkochen, Germany), and five images were taken for each group. Schwann cells were cultured with deposited metallic films in different experimental groups for 3 days. The investigation was performed with the same groups as those for the DRGs, and three independent experiments were conducted for each group ( $n = 3$ ). Schwann cells were then immunostained and investigated following the same procedures as those of DRGs, except that the Schwann cells were immunostained with rabbit anti-NGFp75 antibodies (Sigma-Aldrich, USA) instead of mouse anti-NF200. The length of neurites and the number of Schwann cells are quantified using Image-Pro Plus 6.0 software, and the results are shown as mean  $\pm$  SD. The supernatants of Schwann cell culture solutions were collected (three measurements per group), and the concentrations of neurotrophic factors (CNTF, NGF, VEGF, and BDNF) were analyzed through ELISA kits (Shanghai Jianglai Industrial Co. Ltd., China).

### Calcium imaging of DRG neurons

Rat DRG neurons were dissociated and cultured for 2 weeks as previously described (57). Before imaging, DRG neurons were incubated in loading solution for 30 min and then washed twice in recording solution for 2 min each time, covered by a dark box. Loading solution was made by adding 5  $\mu\text{M}$  Fluo-8 AM (AAT Bioquest, Sunnyvale, CA, USA) in recording solution (145 mM NaCl, 3.6 mM KCl, 1.3 mM  $\text{CaCl}_2$ , 10 mM H-Hepes, and 10 mM glucose). Then, the cells were transferred in a recording chamber and imaged with a fluorescence microscope (BX51WI, Olympus, Tokyo, Japan) equipped with a 60 $\times$  water-immersion objective and an sCMOS (scientific complementary metal-oxide semiconductor) camera (ORCA Flash 4.0, Hamamatsu, Hamamatsu-shi, Japan). A fluorescent light source (Lambda HPX-L5, Sutter Instrument, Novato, CA, USA) was controlled, and the images were acquired using Micro-Manager software (National Institutes of Health, version 1.6) (58), with an exposure time of 50 ms and a sample interval of 5 s. The spontaneous calcium signals in the cell soma were monitored to evaluate the excitability of the DRG neurons by investigating the number and amplitude of calcium waves within 250 s for individual neurons. The investigated cell number is 57 and 80 for the control and E-active groups, respec-

tively. The amplitude (relative change) of calcium waves was calculated with the following equation:  $\Delta F/F_0 = (F - F_0)/F_0$ . Data were managed and analyzed using Excel 2016 (Microsoft, Seattle, WA, USA) and Prism 6 (GraphPad Software, San Diego, CA, USA). The statistical difference was justified by unpaired *t* test ( $*P < 0.05$  and  $**P < 0.01$ ).

### Surgical procedure

All procedures associated with the animal studies are in accordance with the institutional guidelines of the Chinese PLA General Hospital, Beijing, China. The experimental protocol was reviewed and approved by the institutional animal care and use committee at the Chinese PLA General Hospital, Beijing, China (approval number 2016-x9-07). A total of 55 healthy male SD rats (aged 8 weeks, 150 to 180 g) were kept in the experimental animal center of the Chinese PLA General Hospital. The rats were randomly divided into five experimental groups: E-active (electroactive device, conduit with galvanic cells), autograft, hollow (conduit without metallic films), Mg (conduit with only Mg films on both sides), and FeMn (conduit with only FeMn films on both sides). Electrospun PCL layer was present on the inner surface of the conduits of the hollow, Mg, and FeMn groups, and the only difference between the hollow and E-active groups was the absence of galvanic cells. As the gold standard for nerve repair, autograft was used as a reference to assess the therapeutic effects of electroactive conduit devices and to compare with other reported works. During surgery, all rats were anesthetized via injection of sodium pentobarbital solution (1%, 0.3 ml/100 g body weight), and the hair of the right femur was removed. Next, the sciatic nerve of the right hind leg was exposed by making a skin incision and splitting the muscles, and a segment of the nerve was sharply cut and removed under a surgical microscope, creating a 10-mm gap after the retraction of the nerve ends. In the autograft group, the gaps were bridged by the reversed excised nerves. In the other groups, the gaps were bridged using various conduits. The autologous nerves and conduits were coapted proximally and distally using 8-0 surgical sutures, and the muscle and skin were then closed with sutures. All rats were then housed and fed with food and water, and all changes were monitored.

### MRI and micro-CT imaging

MRI of anesthetized rats was performed on a 7.0 T MRI system (Bruker BioSpec 70/20 USR, Germany) with body temperature maintained at 37°C by a circulating water tank, and respiratory rates were monitored together with an electrocardiogram module during the experiments. MRI imaging was performed with rats implanted with electroactive conduit device for 7 days. The T2-weighted images were obtained with a fast spin echo (T2\_TurboRARE) sequence using the following parameters: repetition time/echo time = 3500/40 ms, flip angle = 90, field of view = 50  $\times$  40 mm, matrix = 200  $\times$  160, number of excitation = 10, slice thickness = 1 mm, slice = 30, and acquisition time = 9 min and 20 s. Monitoring of nerve regeneration was also performed using the Quantum GX  $\mu\text{CT}$  System (PerkinElmer, Waltham, USA). Images were acquired with 70 kV, and the projection data were reconstructed with the Quantum GX  $\mu\text{CT}$  Workstation (PerkinElmer, Waltham, USA). Monitoring of rats implanted with electroactive conduit devices was performed for 12 days.

### Immunohistochemical and historical assessment of regenerated nerve tissues

Three to five SD rats were randomly selected from each group at 3, 9, and 12 weeks postoperatively and sacrificed by intra-abdominal

injection of excessive pentobarbital sodium solution ( $n = 3$  for each group at 3 and 9 weeks and  $n = 5$  for each group at 12 weeks). Nerve tissues were removed, and these specimens were fixed in paraformaldehyde solutions (4%) for 12 hours, followed by soaking in sucrose solutions (30%) for 48 hours. By using a frozen slicer (Leica, Wetzlar, Germany), nerve tissues were cut transversely into 10- $\mu\text{m}$  sections at different locations (fig. S13): one-half section (3 weeks), two-third and distal sections (9 weeks), and one-half section (12 weeks). The sections are randomly divided into two groups: one for immunofluorescent staining and the other for H&E staining. For immunofluorescent staining, sections were washed with PBS for three times and incubated with normal goat serum (10%; Solarbio, China) at room temperature for 30 min. They were then stained with mouse anti-NF200 antibodies (Sigma-Aldrich Inc., USA) and rabbit anti-S100 antibodies (Sigma-Aldrich Inc., USA) overnight at 4°C and then with secondary antibodies goat anti-rabbit (IgG H+L, Alexa Fluor 594, Abcam, USA) and goat anti-mouse (IgG H+L, Alexa Fluor 488, Abcam, USA) at room temperature for 1 hour in the dark. After washing with PBS, the sections were stained with DAPI and incubated at room temperature for 5 min. The stained sections were rinsed with water and sealed with water-based sealants. The other sections are used for H&E staining. The H&E-stained sections were observed under a slide scanning system (Pannoramic SCAN, 3DHISTECH, Budapest, Hungary), and the other stained sections were observed (five images for each group) under a laser confocal microscope (LSM 710, Zeiss, Oberkochen, Germany).

### TEM investigation of myelinated nerve fibers

Regenerated nerves at 12 weeks postoperatively were collected at the distal end. They were cold-fixed with glutaraldehyde (2.5%) for 3 hours and post-fixed in an osmium tetroxide solution (1%) for 1 hour, followed by washing, dehydration, and embedding in Epon 812 epoxy resin. Ultrathin sections (70 nm) were then prepared for TEM observation. Ten images were collected for each sample, and Image-Pro Plus 6.0 software was used to quantify the average g-ratio (area-based), the average diameter of myelinated nerve fibers, and the average thickness of myelin sheath.

### Gastrocnemius muscle evaluation

Five SD rats of each group were selected for investigation of electrophysiological response, elasticity, wet weight ratio, and muscle fiber area of gastrocnemius at 12 weeks postoperatively. Motor nerve function was evaluated by electrophysiological assessment through a PowerLab 4SP distal data acquisition system (Keypoint 3.02, Denmark). The sciatic nerves at the injured side were carefully exposed under anesthesia with sodium phenobarbital (1%). Electrical stimulation (3.0 mA, 1 Hz) was applied at the proximal and distal nerve stumps, and the CMAPs were recorded at the gastrocnemius muscle. The peak amplitudes and latencies of CMAP were calculated and compared among different groups. Ultrasonography was performed to assess the elasticity of gastrocnemius muscle at the injured side, using an Aplio 500 instrument (2 to 10 MHz, Toshiba, Japan) fitted with a linear array probe. Shear wave elasticity was performed to measure changes in the stiffness of gastrocnemius muscles. Briefly, the system was switched to the speed propagation graph mode as images were stabilized and frozen in continuous excitation mode. The elastic modulus was then calculated for images exhibiting good timelines. Three data points were obtained for each sample. Gastrocnemius muscles of both the injured and contralat-

eral hindlimbs were removed and weighted immediately to calculate the wet weight ratio. Gastrocnemius muscles were then fixed with paraformaldehyde (4%) for 12 hours at 4°C and then cut transversely to obtain paraffin sections (thickness, 5  $\mu\text{m}$ ) for Masson's trichrome staining. The stained sections were observed with a light microscope (BX51, Olympus, Tokyo, Japan), and 10 images were taken for each sample. Image-Pro Plus 6.0 software was used to quantify the cross-sectional area of gastrocnemius fibers.

### CatWalk gait analysis system

The CatWalk XT 10.6 gait analysis system (Noldus, Wageningen, The Netherlands) was used to assess the motor function recovery at 2, 4, 6, 8, 10, and 12 weeks postoperatively (the number of SD rats for each group at each time point was 11, 8, 8, 8, 5, and 5, respectively). The walking track was captured as each rat passed the runway by a high-speed camera under the runaway, and the contact area, stand time, and impact intensities of the right injured hind paw and the normal left hind paw were recorded by the CatWalk XT 10.6 analysis software (Noldus, Wageningen, The Netherlands). The 3D plantar pressure distribution was also obtained by measuring the relative intensity of the scattered light brightness in the CatWalk XT 10.6 gait analysis system. Analyses were performed with the same software. The SFI was calculated using the following formula as described previously (56)

$$\text{SFI} = \frac{109.5(\text{ETS} - \text{NTS})}{\text{NTS}} - \frac{38.3(\text{EPL} - \text{NPL})}{\text{NPL}} + \frac{13.3(\text{EIT} - \text{NIT})}{\text{NIT}} - 8.8 \quad (1)$$

where ETS indicates the experimental toe spread (distance between the first and fifth toes), NTS indicates the normal toe spread, EIT indicates the experimental intertoe spread (the distance between the second and fourth toes), NIT indicates the normal intertoe spread, EPL indicates the experimental print length, and NPL indicates the normal print length. Evaluations were performed by an investigator blinded to the experimental group.

### Statistical analysis

GraphPad Prism (version 6.0) was used for the statistical analysis followed by unpaired  $t$  test ( $*P < 0.05$  and  $**P < 0.01$ ) for calcium activity. The SPSS software package (version 23.0) was used for the other statistical analysis, followed by one-way analysis of variance (ANOVA) ( $*P < 0.05$  and  $**P < 0.01$ ). Data are given in boxplots, where the center line is the median, the upper and lower edges of the box are the third and first quartiles, respectively, and the limits of the upper and lower whiskers are the largest and smallest values that are equal or less than 1.5 times of the interquartile range, respectively.

### SUPPLEMENTARY MATERIALS

Supplementary material for this article is available at <http://advances.sciencemag.org/cgi/content/full/6/50/eabc6686/DC1>

### REFERENCES AND NOTES

1. J. Noble, C. A. Munro, V. S. S. V. Prasad, R. Midha, Analysis of upper and lower extremity peripheral nerve injuries in a population of patients with multiple injuries. *J. Trauma* **45**, 116–122 (1998).
2. J. S. Belkas, M. S. Shoichet, R. Midha, Axonal guidance channels in peripheral nerve regeneration. *Oper. Tech. Orthop.* **14**, 190–198 (2004).
3. E. O. Johnson, P. N. Soucacos, Nerve repair: Experimental and clinical evaluation of biodegradable artificial nerve guides. *Injury* **39**, 30–36 (2008).

4. A. N. Koppes, A. L. Nordberg, G. M. Paolillo, N. M. Goodsell, H. A. Darwish, L. Zhang, D. M. Thompson, Electrical stimulation of Schwann cells promotes sustained increases in neurite outgrowth. *Tissue Eng. Part A* **20**, 494–506 (2014).
5. W. Z. Ray, S. E. Mackinnon, Management of nerve gaps: Autografts, allografts, nerve transfers, and end-to-side neurotaphy. *Exp. Neurol.* **223**, 77–85 (2010).
6. M. E. Ortigiñela, M. B. Wood, D. R. Cahill, Anatomy of the sural nerve complex. *J. Hand Surg. Am.* **12**, 1119–1123 (1987).
7. S. Kehoe, X. F. Zhang, D. Boyd, FDA approved guidance conduits and wraps for peripheral nerve injury: A review of materials and efficacy. *Injury* **43**, 553–572 (2012).
8. G. R. D. Evans, K. Brandt, S. Katz, P. Chauvin, L. Otto, M. Bogle, B. Wang, R. K. Meszlenyi, L. Lu, A. G. Mikos, C. W. Patrick Jr., Bioactive poly (l-lactic acid) conduits seeded with Schwann cells for peripheral nerve regeneration. *Biomaterials* **23**, 841–848 (2002).
9. M. Georgiou, J. P. Golding, A. J. Loughlin, P. J. Kingham, J. B. Phillips, Engineered neural tissue with aligned, differentiated adipose-derived stem cells promotes peripheral nerve regeneration across a critical sized defect in rat sciatic nerve. *Biomaterials* **37**, 242–251 (2015).
10. N. B. Fadia, J. M. Bliley, G. A. DiBernardo, D. J. Crammond, B. K. Schilling, W. N. Sivak, A. M. Spiess, K. M. Washington, M. Waldner, H.-T. Liao, I. B. James, D. M. Minter, C. Tompkins-Rhoades, A. R. Cottrill, D.-Y. Kim, R. Schweizer, D. A. Bourne, G. E. Panagis, M. A. Schusterman II, F. M. Egro, I. K. Campwala, T. Simpson, D. J. Weber, T. Gause II, J. E. Brooker, T. Josyula, A. A. Guevara, A. J. Repko, C. M. Mahoney, K. G. Marra, Long-gap peripheral nerve repair through sustained release of a neurotrophic factor in nonhuman primates. *Sci. Transl. Med.* **12**, eaav7753 (2020).
11. S. Madduri, M. Papaloizos, B. Gander, Synergistic effect of GDNF and NGF on axonal branching and elongation in vitro. *Neurosci. Res.* **65**, 88–97 (2009).
12. A. Faroni, S. A. Mobasser, P. J. Kingham, A. J. Reid, Peripheral nerve regeneration: Experimental strategies and future perspectives. *Adv. Drug Deliv. Rev.* **82–83**, 160–167 (2015).
13. J. Huang, Y. Zhang, L. Lu, X. Hu, Z. Luo, Electrical stimulation accelerates nerve regeneration and functional recovery in delayed peripheral nerve injury in rats. *Eur. J. Neurosci.* **38**, 3691–3701 (2013).
14. T. Gordon, A. W. English, Strategies to promote peripheral nerve regeneration: Electrical stimulation and/or exercise. *Eur. J. Neurosci.* **43**, 336–350 (2016).
15. L. Ghasemi-Mobarakeh, M. P. Prabhakaran, M. Morshed, M. H. Nasr-Esfahani, H. Baharvand, S. Kiani, S. S. Al-Deyab, S. Ramakrishna, Application of conductive polymers, scaffolds and electrical stimulation for nerve tissue engineering. *J. Tissue Eng. Regen. Med.* **5**, e17–e35 (2011).
16. T. Gordon, Electrical stimulation to enhance axon regeneration after peripheral nerve injuries in animal models and humans. *Neurotherapeutics* **13**, 295–310 (2016).
17. X. Zhang, N. Xin, L. Tong, X.-J. Tong, Electrical stimulation enhances peripheral nerve regeneration after crush injury in rats. *Mol. Med. Rep.* **7**, 1523–1527 (2013).
18. Y. Deng, Y. Xu, H. Liu, H. Peng, Q. Tao, H. Liu, H. Liu, J. Wu, X. Chen, J. Fan, Electrical stimulation promotes regeneration and re-myelination of axons of injured facial nerve in rats. *Neurol. Res.* **40**, 231–238 (2018).
19. C. Calvey, W. Zhou, K. S. Stakleff, P. Sendelbach-Sloan, A. B. Harkins, W. Lanzinger, R. K. Willits, Short-term electrical stimulation to promote nerve repair and functional recovery in a rat model. *J. Hand Surg. Am.* **40**, 314–322 (2015).
20. A. A. Al-Majed, C. M. Neumann, T. M. Brushart, T. Gordon, Brief electrical stimulation promotes the speed and accuracy of motor axonal regeneration. *J. Neurosci.* **20**, 2602–2608 (2000).
21. Y. Zhao, Y. Liang, S. Ding, K. Zhang, H.-q. Mao, Y. Yang, Application of conductive PPy/SF composite scaffold and electrical stimulation for neural tissue engineering. *Biomaterials* **255**, 120164 (2020).
22. W. Jing, Y. Zhang, Q. Cai, G. Chen, L. Wang, X. Yang, W. Zhong, Study of electrical stimulation with different electric-field intensities in the regulation of the differentiation of PC12 cells. *ACS Chem. Neurosci.* **10**, 348–357 (2018).
23. S. Meng, Nerve cell differentiation using constant and programmed electrical stimulation through conductive non-functional graphene nanosheets film. *J. Tissue Eng. Regen. Med.* **11**, 274–283 (2014).
24. A. N. Koppes, A. M. Seggio, D. M. Thompson, Neurite outgrowth is significantly increased by the simultaneous presentation of Schwann cells and moderate exogenous electric fields. *J. Neural Eng.* **8**, 046023 (2011).
25. J. S. Park, K. Park, H. T. Moon, D. G. Woo, H. N. Yang, K.-H. Park, Electrical pulsed stimulation of surfaces homogeneously coated with gold nanoparticles to induce neurite outgrowth of PC12 cells. *Langmuir* **25**, 451–457 (2008).
26. T. Gordon, P. Eva, G. H. Borschel, Delayed peripheral nerve repair: Methods, including surgical 'cross-bridging' to promote nerve regeneration. *Neural Regen. Res.* **10**, 1540–1544 (2015).
27. T. Gordon, N. Amirjani, D. C. Edwards, K. M. Chan, Brief post-surgical electrical stimulation accelerates axon regeneration and muscle reinnervation without affecting the functional measures in carpal tunnel syndrome patients. *Exp. Neurol.* **223**, 192–202 (2010).
28. J. Koo, M. R. MacEwan, S.-K. Kang, S. M. Won, M. Stephen, P. Gamble, Z. Xie, Y. Yan, Y.-Y. Chen, J. Shin, N. Birenbaum, S. Chung, S. B. Kim, J. Khalifeh, D. V. Harburg, K. Bean, M. Paskett, J. Kim, Z. S. Zohny, S. M. Lee, R. Zhang, K. Luo, B. Ji, A. Banks, H. M. Lee, Y. Huang, W. Z. Ray, J. A. Rogers, Wireless bioresorbable electronic system enables sustained nonpharmacological neuroregenerative therapy. *Nat. Med.* **24**, 1830–1836 (2018).
29. C. Ju, E. Park, T. Kim, T. Kim, M. Kang, K.-S. Lee, S.-M. Park, Effectiveness of electrical stimulation on nerve regeneration after crush injury: Comparison between invasive and non-invasive stimulation. *PLOS ONE* **15**, e0233531 (2020).
30. Y. Sun, Q. Quan, H. Meng, Y. Zheng, J. Peng, Y. Hu, Z. Feng, X. Sang, K. Qiao, W. He, X. Chi, L. Zhao, Enhanced neurite outgrowth on a multiblock conductive nerve scaffold with self-powered electrical stimulation. *Adv. Healthc. Mater.* **8**, e1900127 (2019).
31. X. Huang, D. Wang, Z. Yuan, W. Xie, Y. Wu, R. Li, Y. Zhao, D. Luo, L. Cen, B. Chen, H. Wu, H. Xu, X. Sheng, M. Zhang, L. Zhao, L. Yin, A fully biodegradable battery for self-powered transient implants. *Small* **14**, e1800994 (2018).
32. L. Yin, X. Huang, H. Xu, Y. Zhang, J. Lam, J. Cheng, J. A. Rogers, Materials, designs, and operational characteristics for fully biodegradable primary batteries. *Adv. Mater.* **26**, 3879–3884 (2014).
33. S. M. Huang, E. A. Nauman, L. A. Stanciu, Investigation of porosity on mechanical properties, degradation and in-vitro cytotoxicity limit of Fe30Mn using space holder technique. *Mater. Sci. Eng. C Mater. Biol. Appl.* **99**, 1048–1057 (2019).
34. Y. F. Zheng, X. N. Gu, F. Witte, Biodegradable metals. *Mater. Sci. Eng. R Rep.* **77**, 1–34 (2014).
35. Y. Liu, Y. Zheng, X.-H. Chen, J.-A. Yang, H. Pan, D. Chen, L. Wang, J. Zhang, D. Zhu, S. Wu, K. W. K. Yeung, R.-C. Zeng, Y. Han, S. Guan, Fundamental theory of biodegradable metals—Definition, criteria, and design. *Adv. Funct. Mater.* **29**, 1805402 (2019).
36. L. Yin, H. Cheng, S. Mao, R. Haasch, Y. Liu, X. Xie, S.-W. Hwang, H. Jain, S.-K. Kang, Y. Su, R. Li, Y. Huang, J. A. Rogers, Dissolvable metals for transient electronics. *Adv. Funct. Mater.* **24**, 645–658 (2014).
37. H. Hermawan, H. Alamdari, D. Mantovani, D. Dubé, Iron–manganese: New class of metallic degradable biomaterials prepared by powder metallurgy. *Powder Metall.* **51**, 38–45 (2008).
38. P. Trumbo, A. A. Yates, S. Schlicker, M. Poos, Dietary reference intakes: Vitamin A, vitamin K, arsenic, boron, chromium, copper, iodine, iron, manganese, molybdenum, nickel, silicon, vanadium, and zinc. *J. Acad. Nutr. Diet.* **101**, 294 (2001).
39. H. Hermawan, D. Dubé, D. Mantovani, Degradable metallic biomaterials: Design and development of Fe–Mn alloys for stents. *J. Biomed. Mater. Res. A* **93**, 1–11 (2010).
40. P. Nadeau, D. El-Damak, D. Glettig, Y. L. Kong, S. Mo, C. Cleveland, L. Booth, N. Roxhed, R. Langer, A. P. Chandrakasan, G. Traverso, Prolonged energy harvesting for ingestible devices. *Nat. Biomed. Eng.* **1**, 0022 (2017).
41. A. Vydyanathan, B. Kosharsky, S. Nair, K. Gritsenko, R. S. Kim, D. Wang, N. Shaparin, The use of electrical impedance to identify intraneural needle placement in human peripheral nerves: A study on amputated human limbs. *Anesth. Analg.* **123**, 228–232 (2016).
42. J. Henley, M.-m. Poo, Guiding neuronal growth cones using Ca<sup>2+</sup> signals. *Trends Cell Biol.* **14**, 320–330 (2004).
43. Z.-Q. Feng, T. Wang, B. Zhao, J. Li, L. Jin, Soft graphene nanofibers designed for the acceleration of nerve growth and development. *Adv. Mater.* **27**, 6462–6468 (2015).
44. A. A. Al-Majed, S. L. Tam, T. Gordon, Electrical stimulation accelerates and enhances expression of regeneration-associated genes in regenerating rat femoral motoneurons. *Cell. Mol. Neurobiol.* **24**, 379–402 (2004).
45. A. A. Al-Majed, T. M. Brushart, T. Gordon, Electrical stimulation accelerates and increases expression of BDNF and trkB mRNA in regenerating rat femoral motoneurons. *Eur. J. Neurosci.* **12**, 4381–4390 (2000).
46. M. P. Willand, M.-A. Nguyen, G. H. Borschel, T. Gordon, Electrical stimulation to promote peripheral nerve regeneration. *Neurorehabil. Neural Repair* **30**, 490–496 (2016).
47. L. F. Jaffe, M.-M. Poo, Neurites grow faster towards the cathode than the anode in a steady field. *J. Exp. Zool.* **209**, 115–128 (1979).
48. C. D. McCaig, Dynamic aspects of amphibian neurite growth and the effects of an applied electric field. *J. Physiol.* **375**, 55–69 (1986).
49. G.-I. Ming, J. Henley, M. Tessier-Lavigne, H.-j. Song, M.-m. Poo, Electrical activity modulates growth cone guidance by diffusible factors. *Neuron* **29**, 441–452 (2001).
50. N. Hirai, H. Ishikawa, Y. Ohki, in *2007 Annual Report-Conference on Electrical Insulation and Dielectric Phenomena* (IEEE, 2007), pp. 592–595.
51. D. W. Lee, S. Yi, Y.-H. Cho, in *18th IEEE International Conference on Micro Electro Mechanical Systems, 2005. MEMS 2005* (IEEE, 2005), pp. 678–681.
52. A. Salmanzadeh, M. B. Sano, R. C. Gallo-Villanueva, P. C. Roberts, E. M. Schmelz, R. V. Davalos, Investigating dielectric properties of different stages of syngeneic murine ovarian cancer cells. *Biomed. Microfluidics* **7**, 011809 (2013).
53. Y. Zheng, J. Nguyen, C. Wang, Y. Sun, Electrical measurement of red blood cell deformability on a microfluidic device. *Lab Chip* **13**, 3275–3283 (2013).
54. C. Lu, Y. Wang, S. Yang, C. Wang, X. Sun, J. Lu, H. Yin, W. Jiang, H. Meng, F. Rao, X. Wang, J. Peng, Bioactive self-assembling peptide hydrogels functionalized

- with brain-derived neurotrophic factor and nerve growth factor mimicking peptides synergistically promote peripheral nerve regeneration. *ACS Biomater Sci. Eng.* **4**, 2994–3005 (2018).
55. J. Du, J. Liu, S. Yao, H. Mao, J. Peng, X. Sun, Z. Cao, Y. Yang, B. Xiao, Y. Wang, P. Tang, X. Wang, Prompt peripheral nerve regeneration induced by a hierarchically aligned fibrin nanofiber hydrogel. *Acta Biomater.* **55**, 296–309 (2017).
  56. Y. Gu, J. Zhu, C. Xue, Z. Li, F. Ding, Y. Yang, X. Gu, Chitosan/silk fibroin-based, Schwann cell-derived extracellular matrix-modified scaffolds for bridging rat sciatic nerve gaps. *Biomaterials* **35**, 2253–2263 (2014).
  57. A. Edelstein, N. Amodaj, K. Hoover, R. Vale, N. Stuurman, Computer control of microscopes using  $\mu$ Manager. *Curr. Protoc. Mol. Biol.* **92**, 14.20.1–14.20.17 (2010).
  58. C. Zhang, W. Xiong, H. Zheng, L. Wang, B. Lu, Z. Zhou, Calcium- and dynamin-independent endocytosis in dorsal root ganglion neurons. *Neuron* **42**, 225–236 (2004).

#### Acknowledgments

**Funding:** This project was supported by the National Natural Science Foundation of China (51601103 to L.Y.), Tsinghua University–Peking Union Medical College Hospital Initiative Scientific Research Program (20191080592 to L.Y.), the China Postdoctoral Science Foundation (2018 M641341 to L.W.), the Beijing Municipal Natural Science Foundation (4202032 to X.S.), the National Key R&D Program of China (2018YFB0704304-1 and 2016YFC1101601), and Medical Research and Development Projects (AWS17J005). **Author**

**contributions:** L.W. and L.Y. conceived the idea. L.W., C.L., Y.W., X.W., X.S., J.P., and L.Y. designed the research project. L.W., P.S., Q.W., J.H., H.C., Y.L., and L.Y. designed and fabricated the devices and performed the analysis. L.W., S.L., S.W., H.H., and W.X. performed the investigation of calcium dynamics. L.W., C.L., S.Y., and Y.G. performed the cell growth tests. L.W., C.L., S.Y., P.S., H.M., Y.G., H.L., W.L., Y. Zhao, J.W., Y. Zhu, D.L., and T.L. performed the animal studies. D.C. and X.S. performed the simulation studies. L.W., P.S., X.S., and L.Y. wrote the manuscript with input from all authors. **Competing interests:** The authors declare that they have no competing interests. **Data and materials availability:** All data needed to evaluate the conclusions in the paper are present in the paper and/or the Supplementary Materials. Additional data related to this paper may be requested from the authors.

Submitted 7 May 2020

Accepted 26 October 2020

Published 11 December 2020

10.1126/sciadv.abc6686

**Citation:** L. Wang, C. Lu, S. Yang, P. Sun, Y. Wang, Y. Guan, S. Liu, D. Cheng, H. Meng, Q. Wang, J. He, H. Hou, H. Li, W. Lu, Y. Zhao, J. Wang, Y. Zhu, Y. Li, D. Luo, T. Li, H. Chen, S. Wang, X. Sheng, W. Xiong, X. Wang, J. Peng, L. Yin, A fully biodegradable and self-electrified device for neuroregenerative medicine. *Sci. Adv.* **6**, eabc6686 (2020).

## A fully biodegradable and self-electrified device for neuroregenerative medicine

Liu Wang, Changfeng Lu, Shuhui Yang, Pengcheng Sun, Yu Wang, Yanjun Guan, Shuang Liu, Dali Cheng, Haoye Meng, Qiang Wang, Jianguo He, Hanqing Hou, Huo Li, Wei Lu, Yanxu Zhao, Jing Wang, Yaqiong Zhu, Yunxuan Li, Dong Luo, Tong Li, Hao Chen, Shirong Wang, Xing Sheng, Wei Xiong, Xiumei Wang, Jiang Peng and Lan Yin

*Sci Adv* 6 (50), eabc6686.  
DOI: 10.1126/sciadv.abc6686

ARTICLE TOOLS	<a href="http://advances.sciencemag.org/content/6/50/eabc6686">http://advances.sciencemag.org/content/6/50/eabc6686</a>
SUPPLEMENTARY MATERIALS	<a href="http://advances.sciencemag.org/content/suppl/2020/12/07/6.50.eabc6686.DC1">http://advances.sciencemag.org/content/suppl/2020/12/07/6.50.eabc6686.DC1</a>
REFERENCES	This article cites 56 articles, 2 of which you can access for free <a href="http://advances.sciencemag.org/content/6/50/eabc6686#BIBL">http://advances.sciencemag.org/content/6/50/eabc6686#BIBL</a>
PERMISSIONS	<a href="http://www.sciencemag.org/help/reprints-and-permissions">http://www.sciencemag.org/help/reprints-and-permissions</a>

Use of this article is subject to the [Terms of Service](#)

---

*Science Advances* (ISSN 2375-2548) is published by the American Association for the Advancement of Science, 1200 New York Avenue NW, Washington, DC 20005. The title *Science Advances* is a registered trademark of AAAS.

Copyright © 2020 The Authors, some rights reserved; exclusive licensee American Association for the Advancement of Science. No claim to original U.S. Government Works. Distributed under a Creative Commons Attribution NonCommercial License 4.0 (CC BY-NC).

## Supplementary Materials for

### **A fully biodegradable and self-electrified device for neuroregenerative medicine**

Liu Wang, Changfeng Lu, Shuhui Yang, Pengcheng Sun, Yu Wang\*, Yanjun Guan, Shuang Liu, Dali Cheng, Haoye Meng, Qiang Wang, Jianguo He, Hanqing Hou, Huo Li, Wei Lu, Yanxu Zhao, Jing Wang, Yaqiong Zhu, Yunxuan Li, Dong Luo, Tong Li, Hao Chen, Shirong Wang, Xing Sheng, Wei Xiong, Xiumei Wang, Jiang Peng\*, Lan Yin\*

\*Corresponding author. Email: lanyin@tsinghua.edu.cn (L.Y.);  
pengjiang301@126.com (J.P.); wangwangdian628@126.com (Y.W.)

Published 11 December 2020, *Sci. Adv.* **6**, eabc6686 (2020)  
DOI: 10.1126/sciadv.abc6686

#### **The PDF file includes:**

Figs. S1 to S27  
Table S1  
Legends for movies S1 to S4

#### **Other Supplementary Material for this manuscript includes the following:**

(available at [advances.sciencemag.org/cgi/content/full/6/50/eabc6686/DC1](https://advances.sciencemag.org/cgi/content/full/6/50/eabc6686/DC1))

Movies S1 to S4

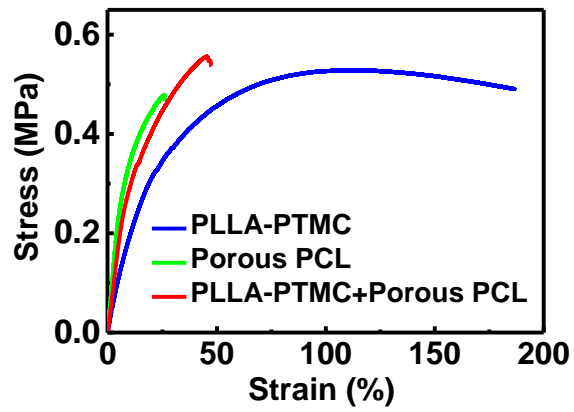


**Figure S1. Tensile tests of PLLA-PTMC (elastic modulus:  $1.45 \pm 0.27$  MPa), porous PCL (elastic modulus:  $5.73 \pm 0.95$  MPa) and porous PCL/PLLA-PTMC bilayer films (elastic modulus:  $3.08 \pm 0.50$  MPa).**

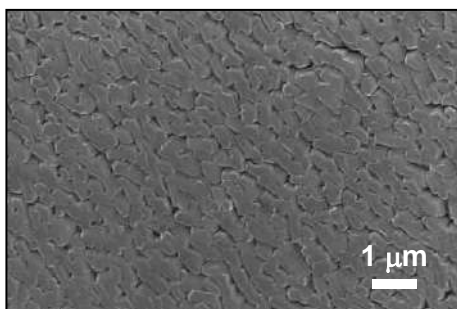


**Figure S2. SEM image of Mg thin films deposited through magnetron sputtering.**

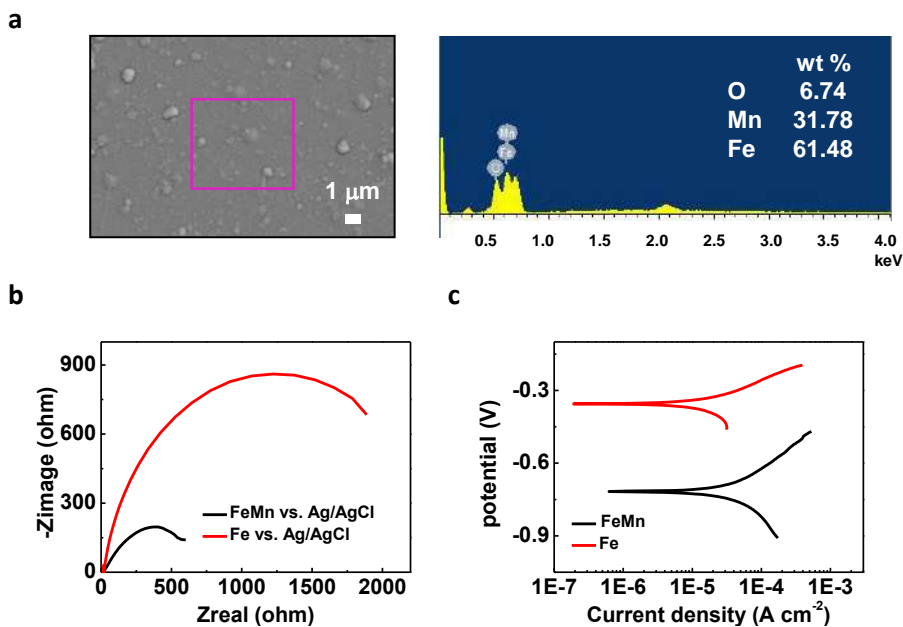


**Figure S3. Characterizations of FeMn thin films.** **a.** SEM image and the energy-dispersive X-ray spectroscopy (EDS) result of FeMn thin film deposited through magnetron sputtering using a customized target (Fe-30 wt% Mn alloy). **b.** Electrochemical impedance spectra of Fe and FeMn alloy in phosphate buffered saline (PBS). (Amplitude: 5 mV, 0 V bias from the open circuit voltage (OCV)) **c.** Galvanodynamic polarization curves of Fe and FeMn alloy in PBS. (scan rate: 0.2 mV/s)

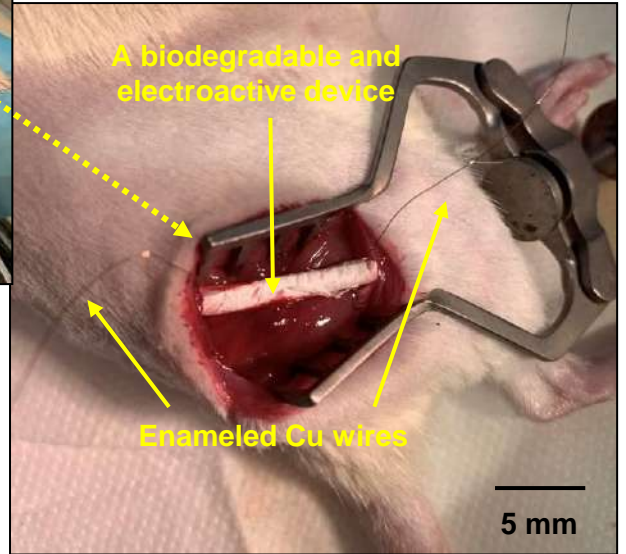
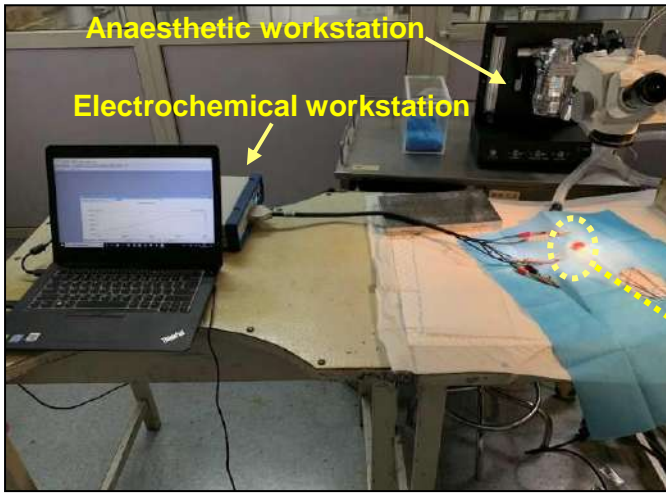


**Figure S4.** Setup for *in vivo* evaluation of the electric field provided by the biodegradable and electroactive conduit device in Sprague-Dawley (SD) rats. Photo Credit: Liu Wang, Tsinghua University.

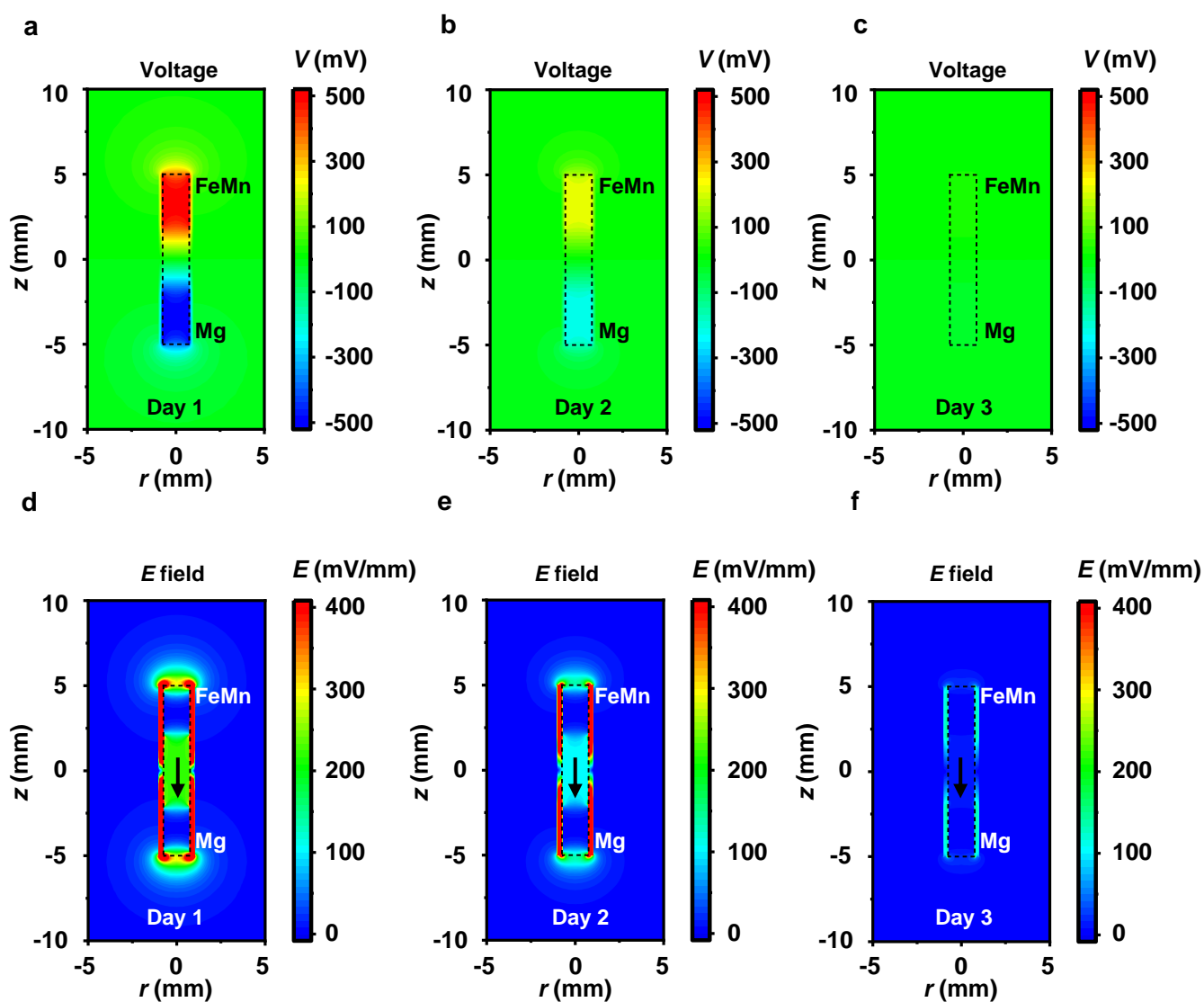


**Figure S5. Finite element analysis of *in vivo* electric field distribution around the electroactive conduit, with input from the measured OCV. a–c. Voltage distribution, after a. 1 day, b. 2 days and c. 3 days. Zero voltage is defined at plane  $z = 0$ , and the voltage drops with time due to the degradation of the electrodes. d–f. Simulated electric field distribution after d. 1 day, e. 2 days and f. 3 days. Black arrows indicate that the electric field dominantly lies on  $-z$  direction inside the conduit (the maximum electric field is confined within the conduit wall). Color contour plots are sectional views of the cylindrical tube crossing the axis, and the black dashed rectangles indicate the inner surface of the electroactive nerve conduit. FeMn cathodes are at the top and Mg anodes are at the bottom.**

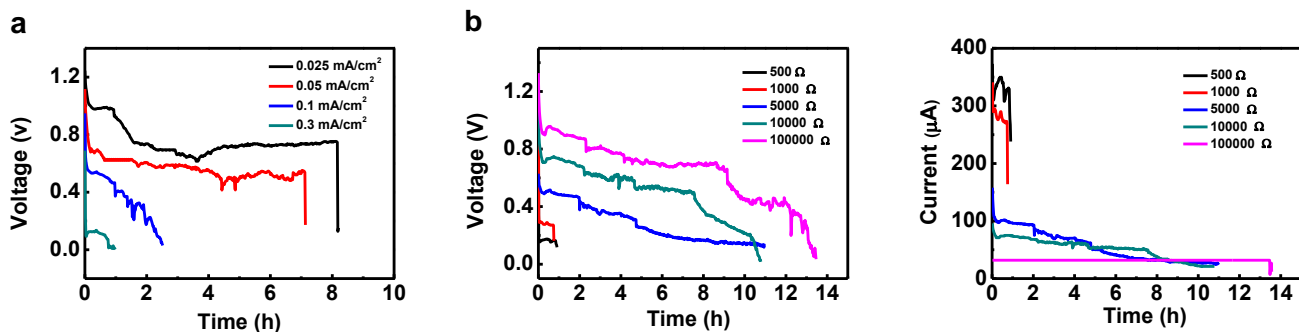


**Figure S6. Representative discharge behavior of a Mg-FeMn galvanic cell in culture media with different current densities and external loads. a.** Discharge behavior with different current densities. **b.** discharge behavior with different external loads. Metallic thin-film electrodes are deposited on PET films, with PLLA-PTMC (~ 50 μm) as the encapsulation layer.

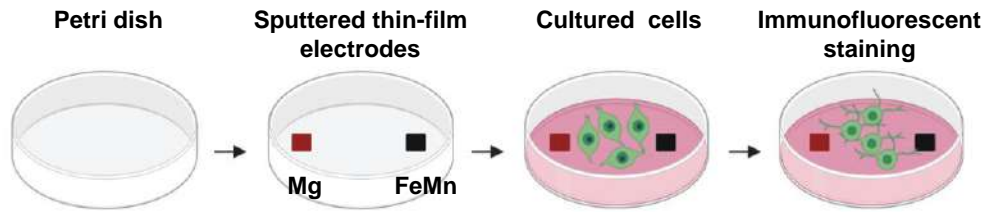


**Figure S7. Experimental setup of *in vitro* cell studies to evaluate cytotoxicity and the effects of the electric field provided by Mg-FeMn galvanic cells. Metallic thin films (with a distance  $\sim 3$  mm) are deposited on petri dish with an encapsulation layer of PLLA-PTMC ( $\sim 50$   $\mu\text{m}$ ). Cells are co-cultured with metallic films. The outgrowth behavior of cells are investigated by immunofluorescent staining and observation is performed with a confocal microscope.**

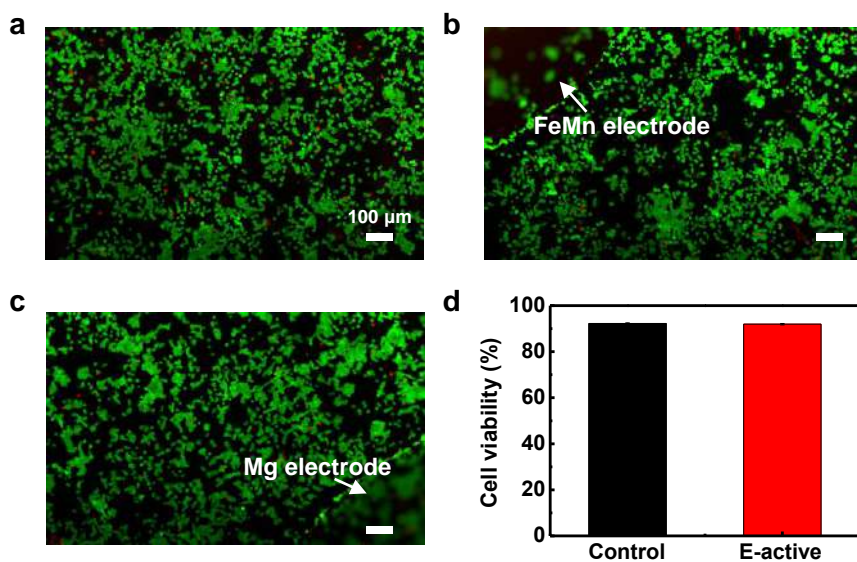


**Figure S8. Cytotoxicity tests of PC12 cells co-cultured with Mg-FeMn galvanic cells. a.** Fluorescent image of the control group. **b.** Fluorescent image at the edge of the FeMn electrode of the E-active group. **c.** Fluorescent image at the edge of the Mg electrode of the E-active group. Green (Calcein-AM) for live cells and red (ethidium homodimer-1, EthD-1) for dead cells. **d.** Cell viability on day 7.  $n = 3$  independent experiments per group.

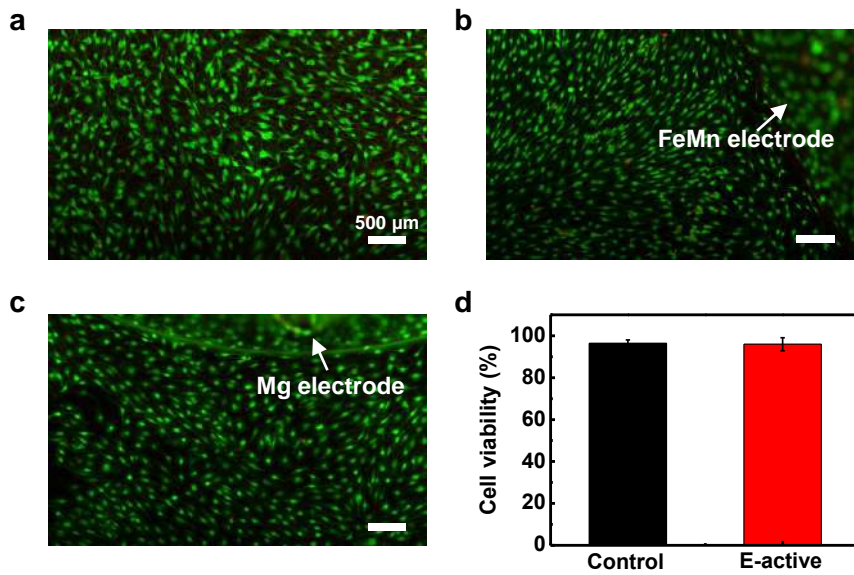


**Figure S9. Cytotoxicity tests of Schwann cells co-cultured with Mg-FeMn galvanic cells. a.** Fluorescent image of the control group. **b.** Fluorescent image at the edge of the FeMn electrode of the E-active group. **c.** Fluorescent image at the edge of the Mg electrode of the E-active group. Green (Calcein-AM) for live cells and red (EthD-1) for dead cells. **d.** Cell viability on day 7.  $n = 3$  independent experiments per group.

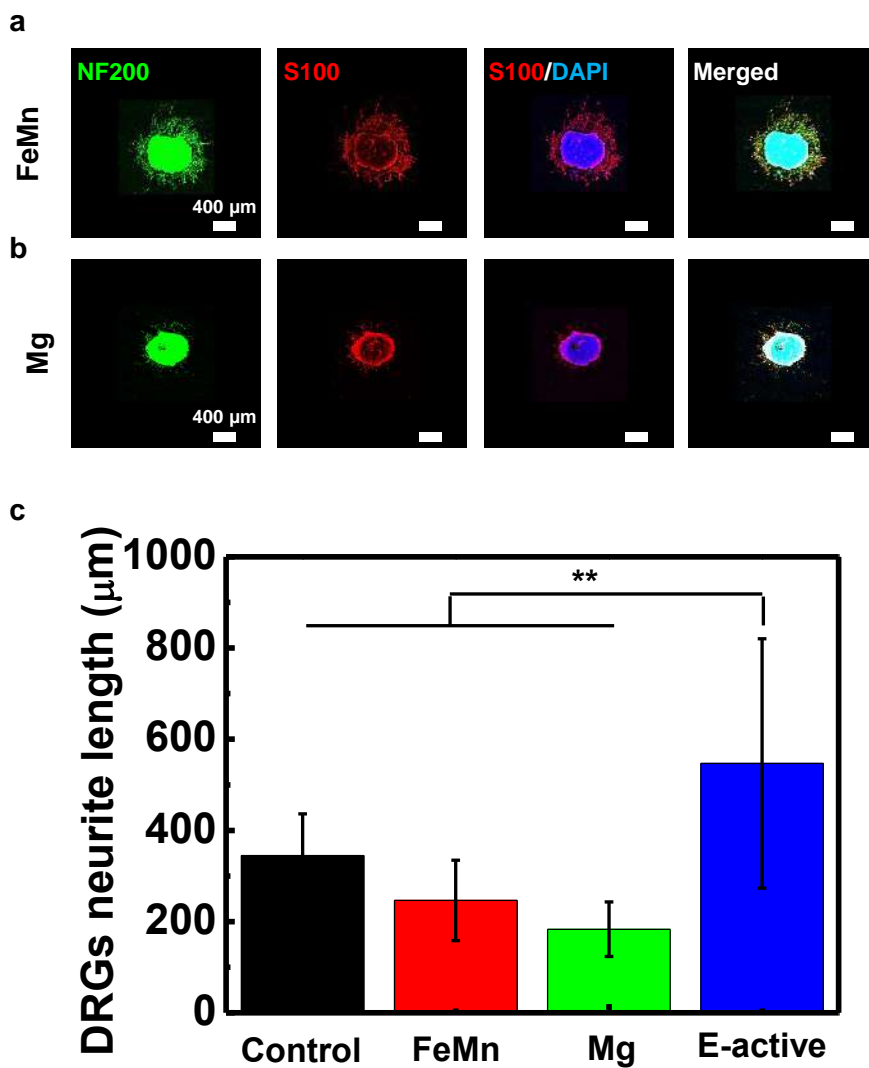


**Figure S10. Influence of Mg-FeMn galvanic cells on the growth behavior of dorsal root ganglion (DRG) neurons.** **a.** Immunofluorescent images of the FeMn group. **b.** Immunofluorescent images of the Mg group. Immunohistochemical staining: axons (NF200, green), Schwann cells (S100, red), and nuclei (4',6-diamidino-2-phenylindole (DAPI), blue). **c.** Statistical analysis of the neurite length of DRGs. (data are mean  $\pm$  s.d.).  $n = 3$  independent experiments per group. The SPSS software package (version 23.0) was used for the statistical analysis followed by one-way analysis of variance (ANOVA) (\*\*  $p < 0.01$ ).

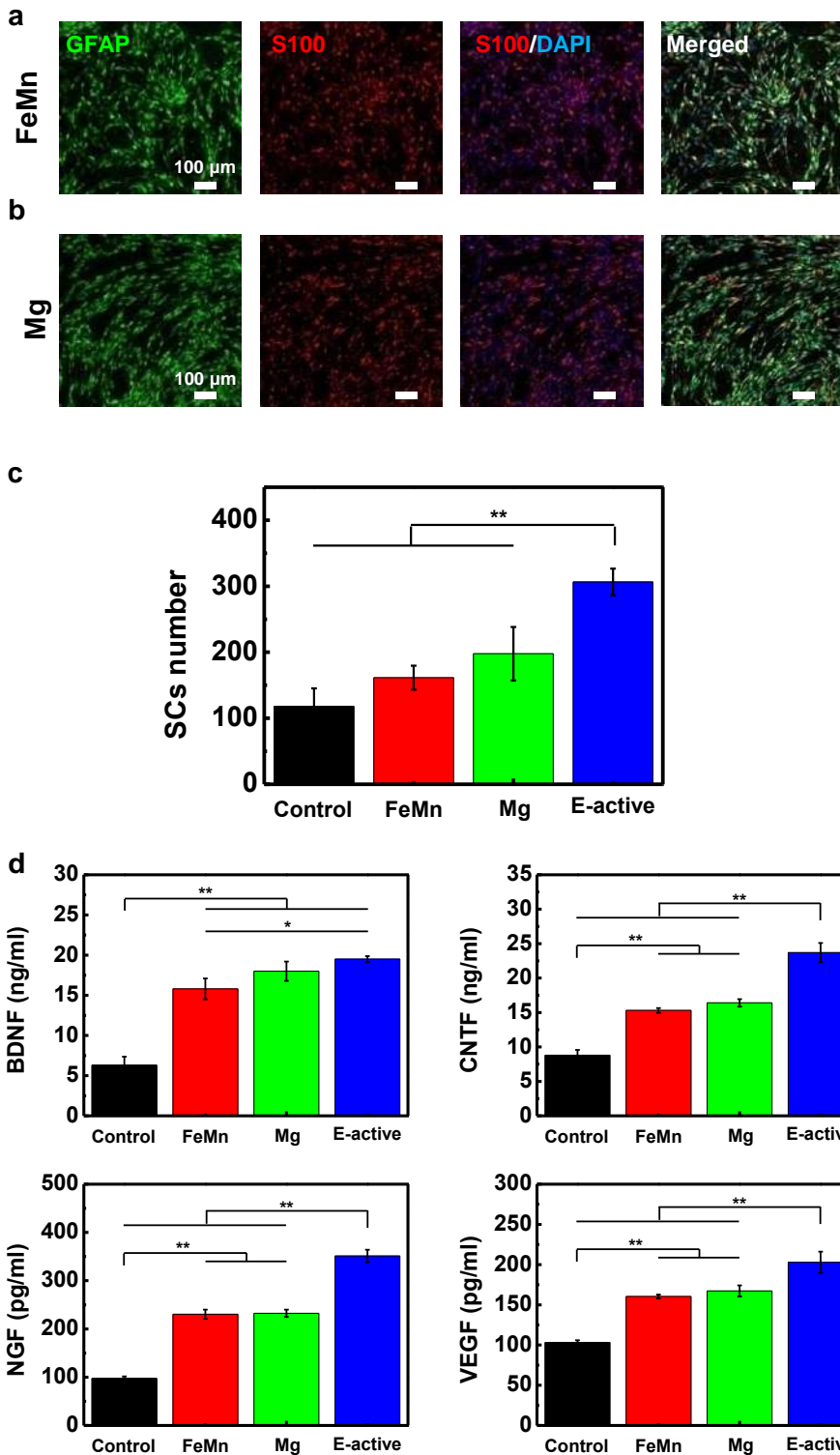


**Figure S11. Influence of Mg-FeMn galvanic cells on the growth behavior of Schwann cells. a.** Confocal microscope images of Schwann cells in the FeMn group. **b.** Confocal microscope images of Schwann cells in the Mg group. Immunohistochemical staining: Schwann cells (glial fibrillary acidic protein (GFAP, green) Schwann cells (S100, red), and nuclei (DAPI, blue). **c.** Statistical analysis of the number of Schwann cells ( $500 \times 500 \mu\text{m}^2$ ). **d.** ELISA of neurotrophic factors: the concentrations of BDNF, CNTF, NGF and VEGF in the supernatants of Schwann cells of all groups. (data are mean  $\pm$  s.d.)  $n = 3$  independent experiments per group. The SPSS software package (version 23.0) was used for the statistical analysis followed by ANOVA (\*  $p < 0.05$ , \*\*  $p < 0.01$ ).

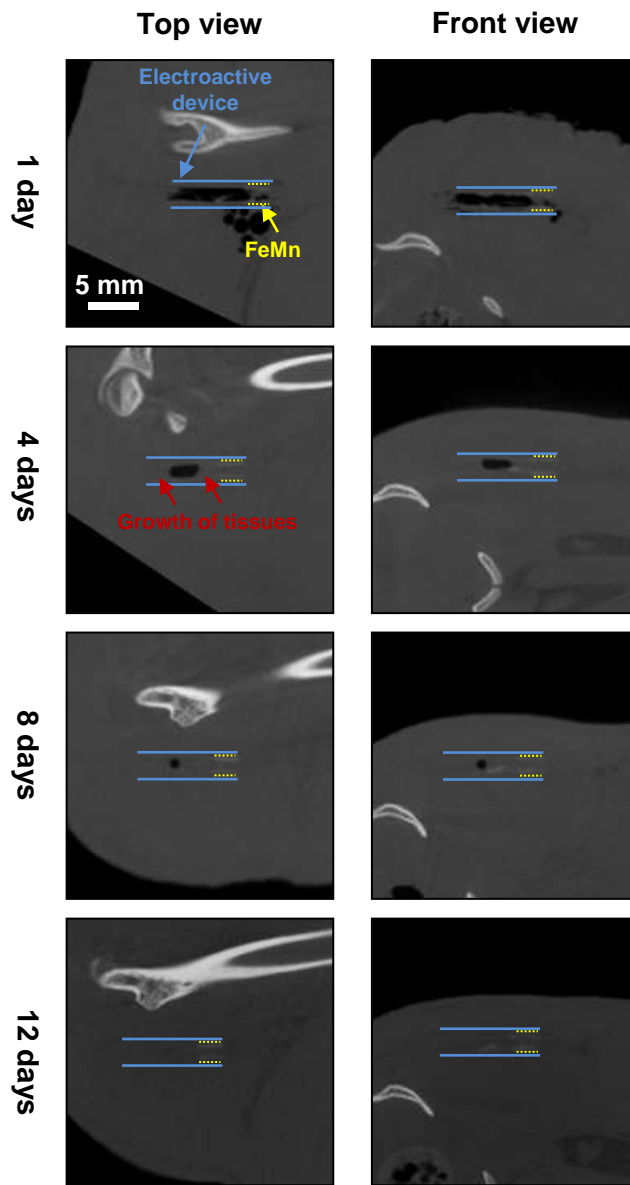


**Figure S12.** Micro-CT images of the E-active group collected at different stages of the nerve regeneration process. The black tube-like region resulting from density difference between the surrounding tissues and empty conduits indicates the location of electroactive devices (marked with blue lines). The white contrast on the electroactive device indicates FeMn thin films (marked with yellow dotted lines).

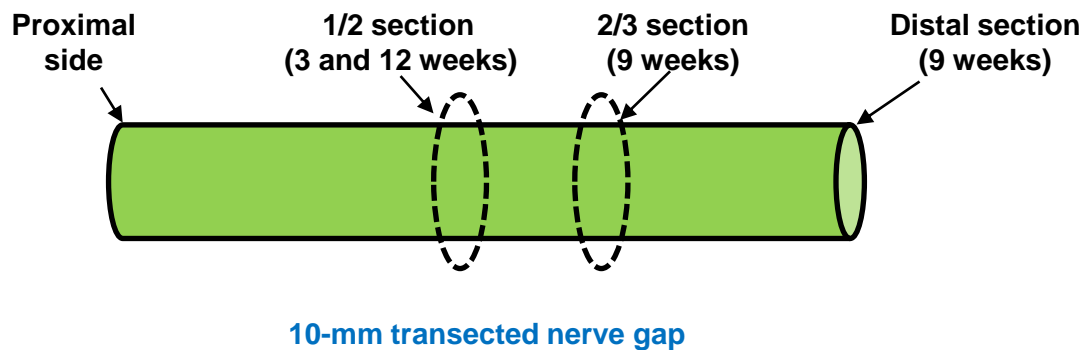


**Figure S13. Schematic of transverse sections at different stages of the nerve regeneration process.**

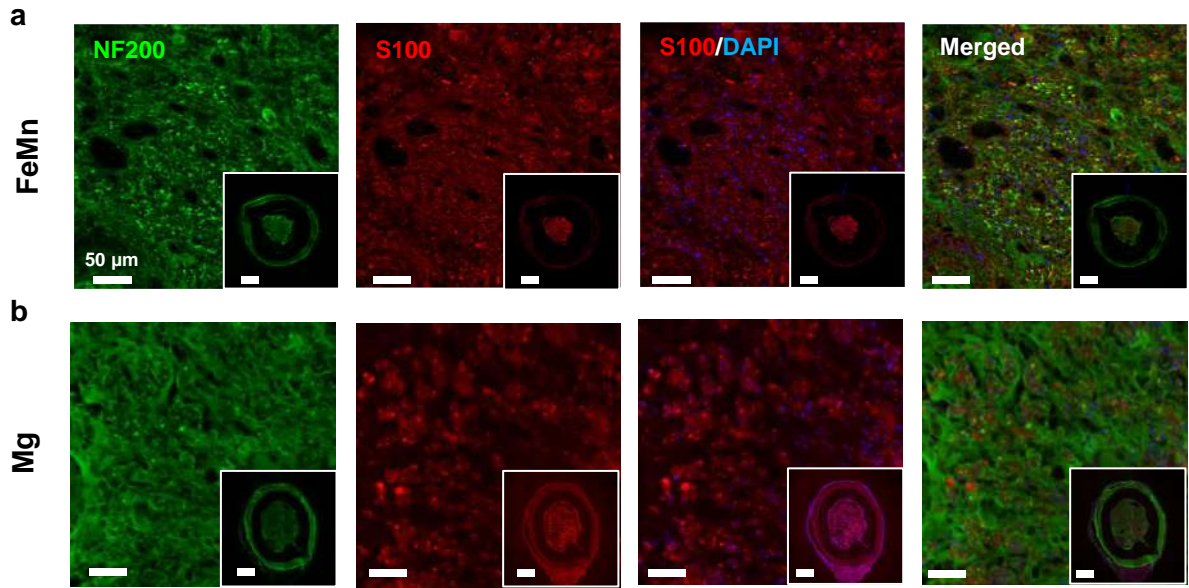


**Figure S14. Immunofluorescent images of the transverse sections of regenerated tissues at the middle of the nerve segment at 3 weeks postimplantation. a. The FeMn group. b. The Mg group. Immunohistochemical staining: axons (NF200, green), Schwann cells (S100, red), and nuclei (DAPI, blue).**

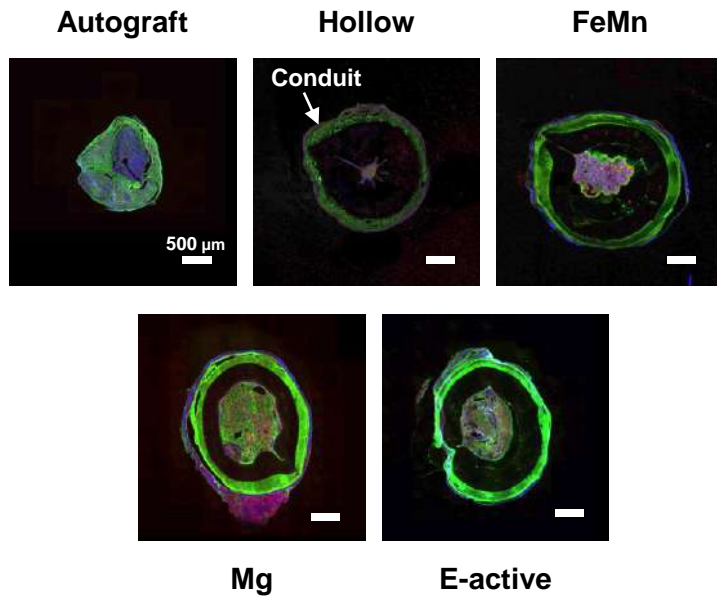


**Figure S15.** Immunofluorescent images of the transverse sections of regenerated tissues at the middle of the nerve segment at 3 weeks postimplantation. Immunohistochemical staining: axons (NF200, green), Schwann cells (S100, red), and nuclei (DAPI, blue).

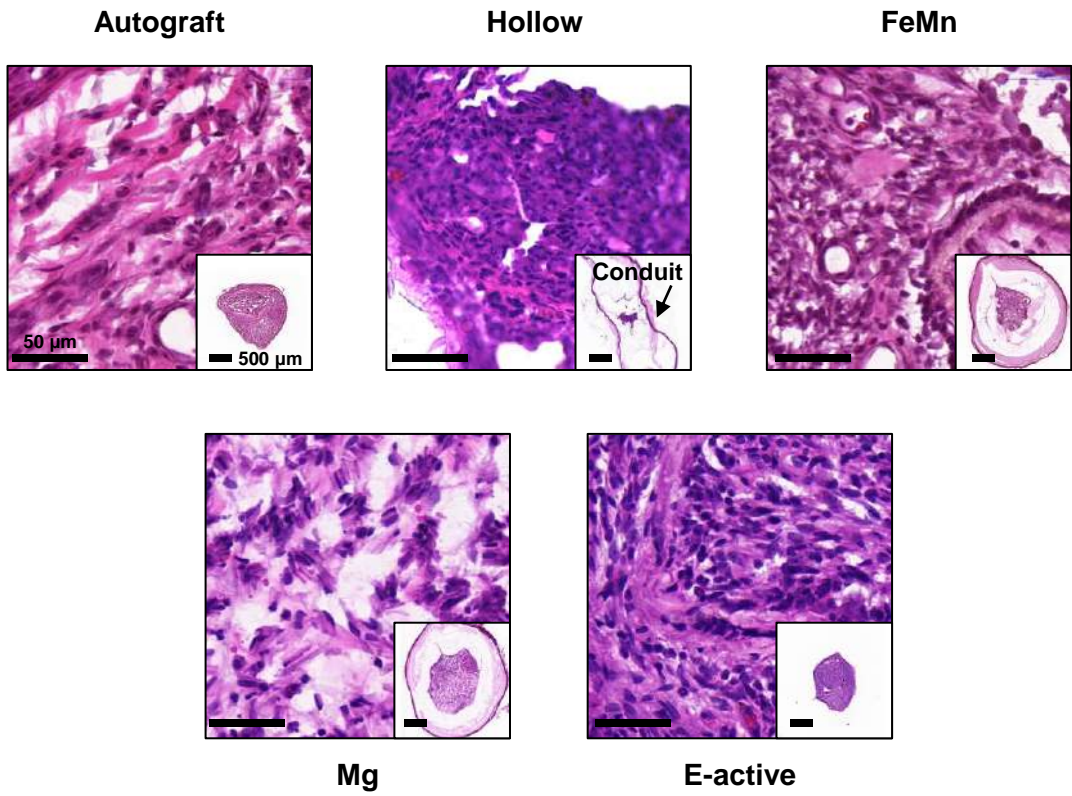


**Figure S16. H&E staining images of the transverse sections of regenerated tissues at the middle of the nerve segment at 3 weeks postimplantation.**

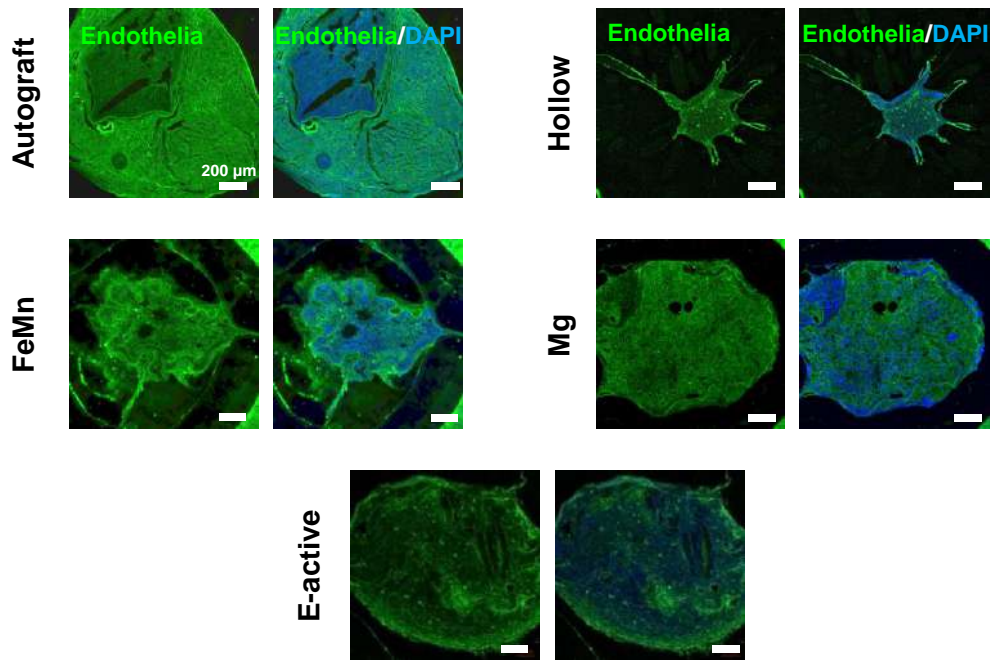


**Figure S17. Immunofluorescent staining images of endothelia cells of the transverse sections of regenerated tissues at the middle of the nerve segment at 3 weeks postimplantation. Immunohistochemical staining: vascular endothelia (Endothelia, green), and nuclei (DAPI, blue).**

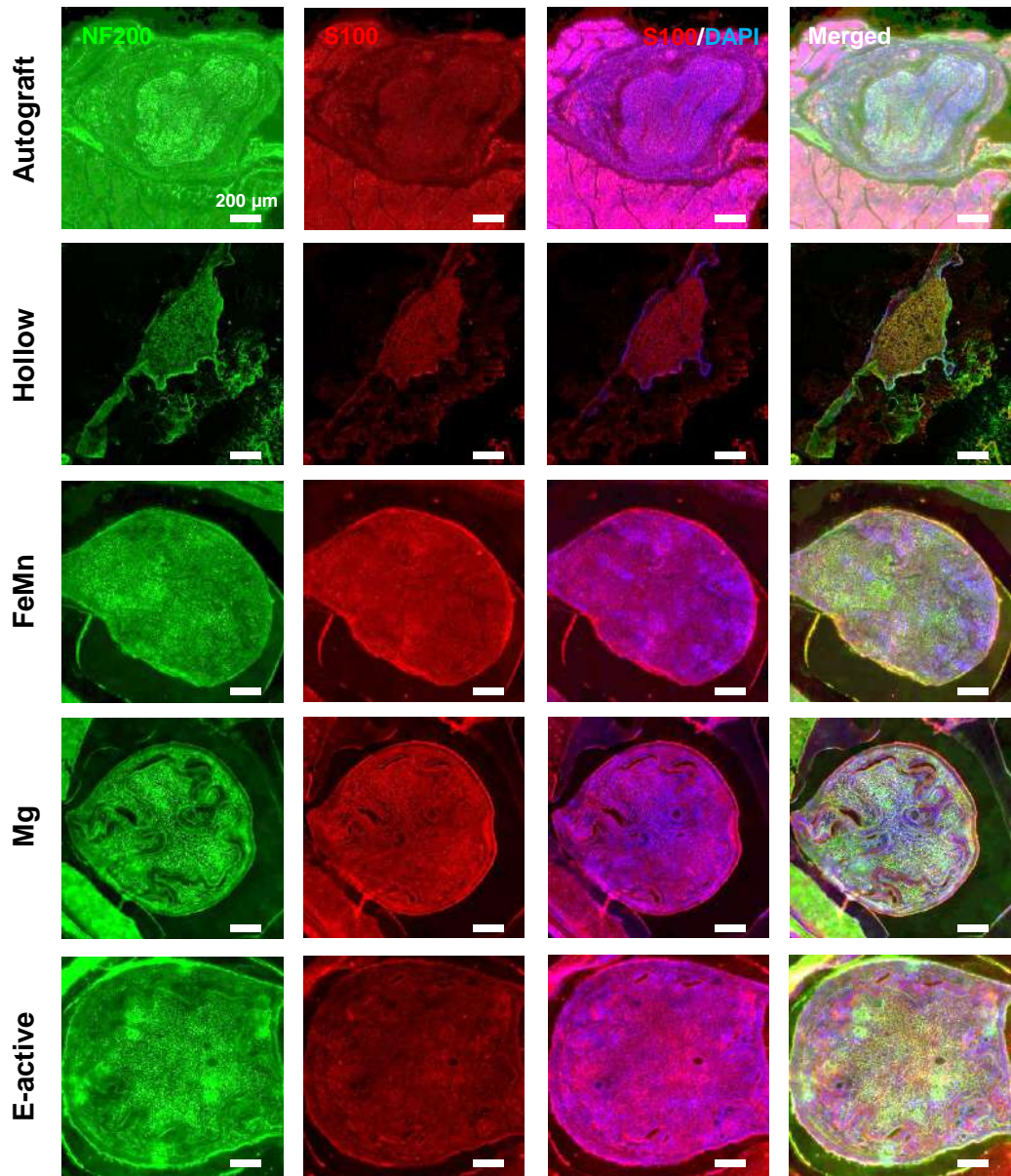
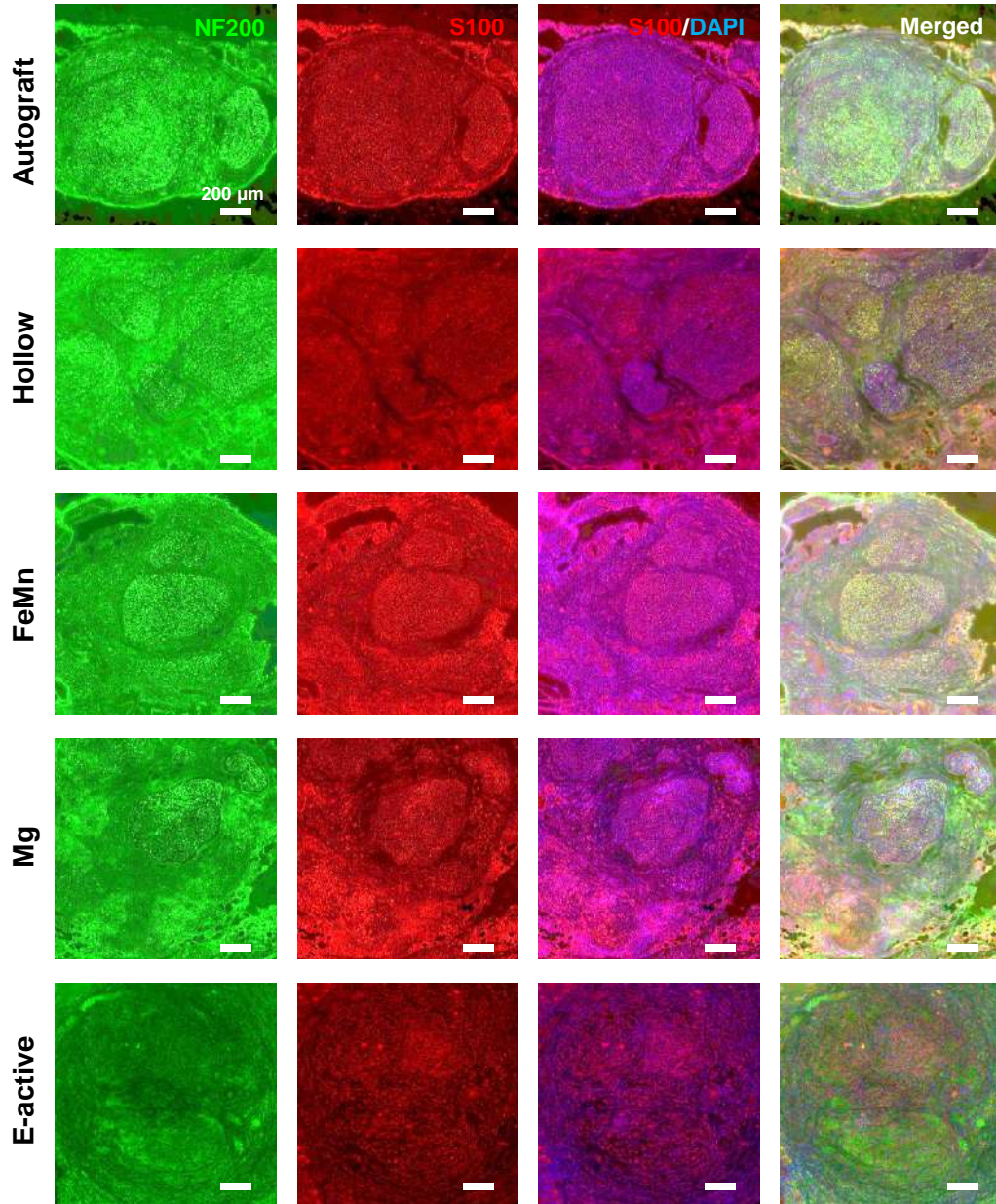
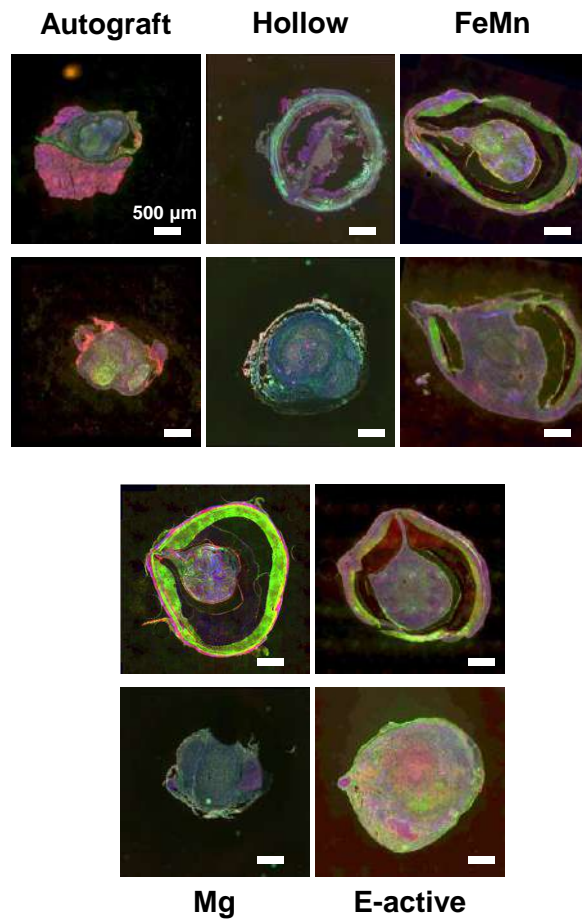


Figure S18. Immunofluorescent images of the transverse sections of regenerated tissues at 9 weeks postimplantation (2/3 section). Immunohistochemical staining: axons (NF200, green), Schwann cells (S100, red), and nuclei (DAPI, blue).



**Figure S19.** Immunofluorescent images of the transverse sections of regenerated tissues at 9 weeks postimplantation (distal section). Immunohistochemical staining: axons (NF200, green), Schwann cells (S100, red), and nuclei (DAPI, blue).



**Figure S20. Immunofluorescent images of the transverse sections of regenerated tissues at 9 weeks postimplantation. (Top: 2/3 section; bottom: distal section). Immunohistochemical staining: axons (NF200, green), Schwann cells (S100, red), and nuclei (DAPI, blue).**

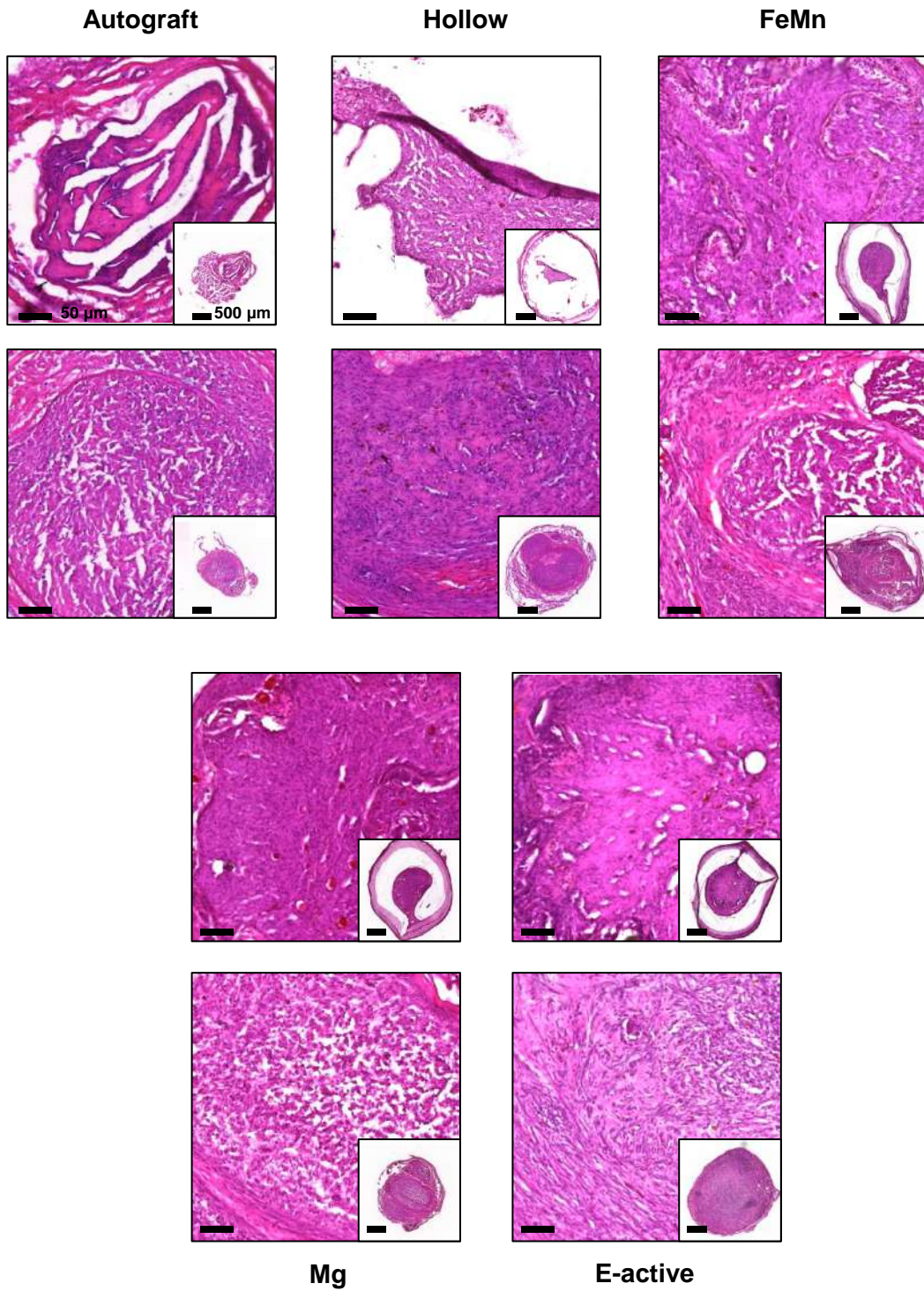


**Figure S21. H&E staining images of the transverse sections of regenerated tissues at 9 weeks postimplantation. (Top: 2/3 section; bottom: distal section).**

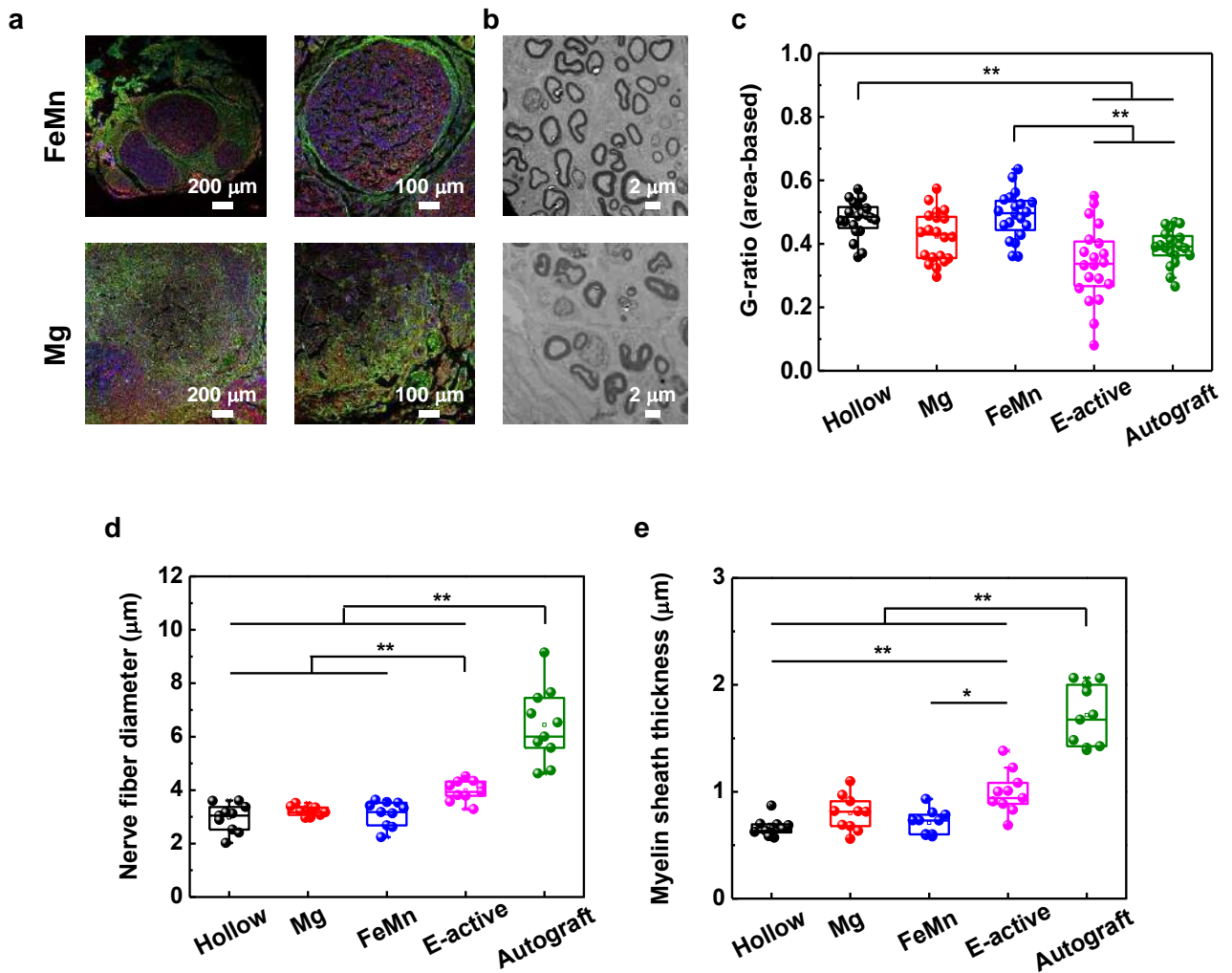


**Figure S22. Evaluation of regenerated nerve tissues at 12 weeks postimplantation.** **a.** Immunofluorescent images of the transverse section at the middle of the nerve segment (1/2 section) of the Mg and FeMn groups. Immunohistochemical staining: axons (NF200, green), Schwann cells (S100, red), and nuclei (DAPI, blue). **b.** TEM images of regenerated nerve tissues. **c.** Statistical results of the average area-based g-ratio. **d.** Statistical results of the average diameters of myelinated nerve fibers. **e.** Statistical results of the average thickness of myelin sheath.  $n = 5$  independent animals per group. The SPSS software package (version 23.0) was used for the statistical analysis followed by ANOVA (\*  $p < 0.05$ , \*\*  $p < 0.01$ ).

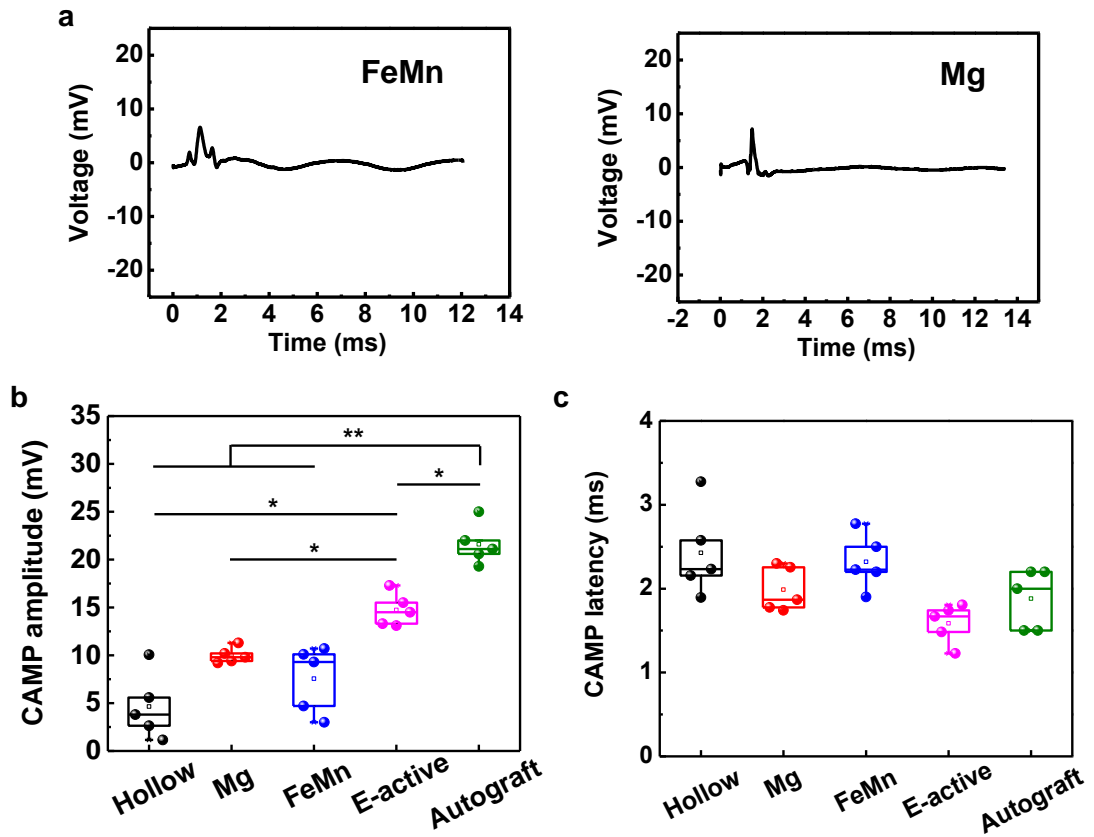


**Figure S23. Electrophysiological tests at 12 weeks postimplantation.** **a.** Representative CMAP recording at the injured side in the FeMn and Mg groups. **b.** CMAP amplitude at the injured side. **c.** CMAP latency at the injured side.  $n = 5$  independent animals per group. The SPSS software package (version 23.0) was used for the statistical analysis followed by ANOVA (\*  $p < 0.05$ , \*\*  $p < 0.01$ ).

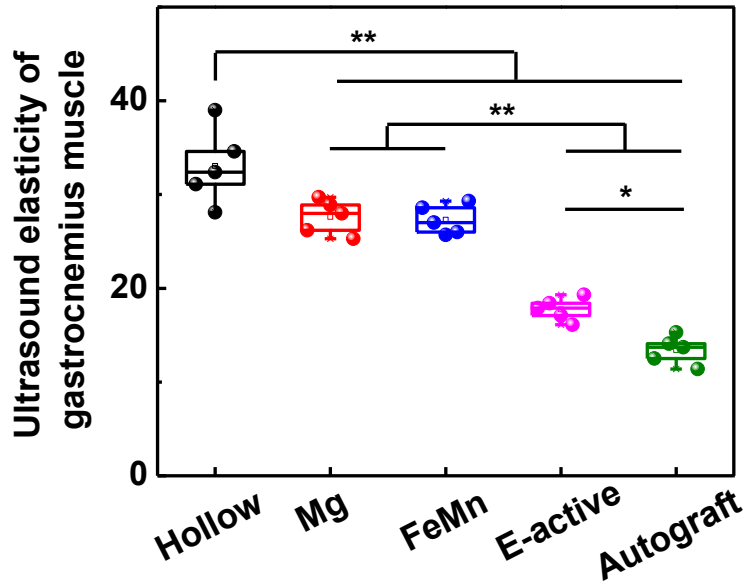
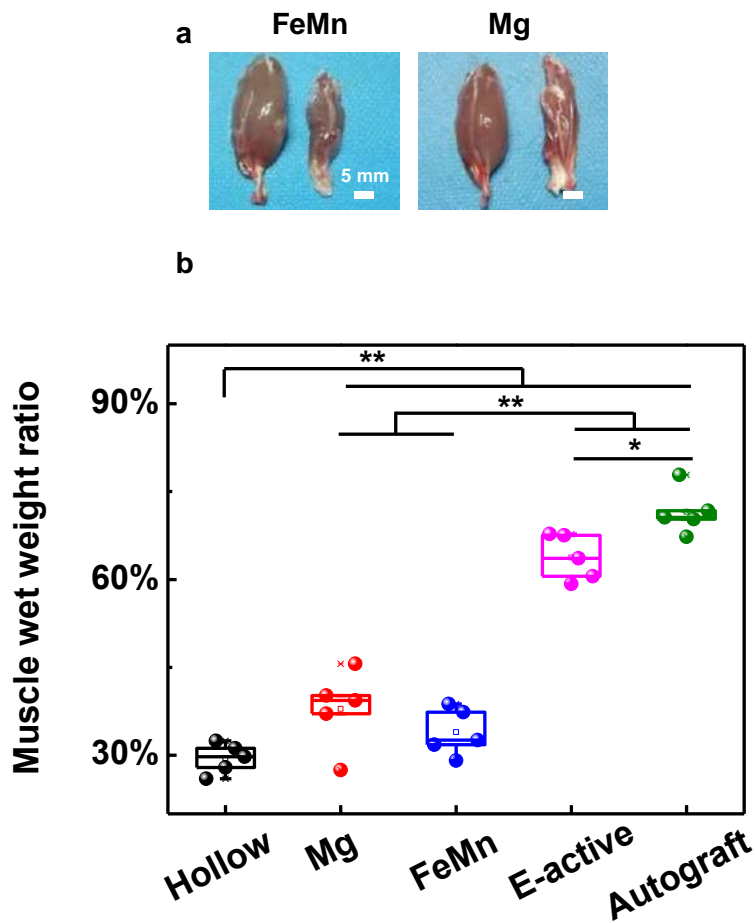
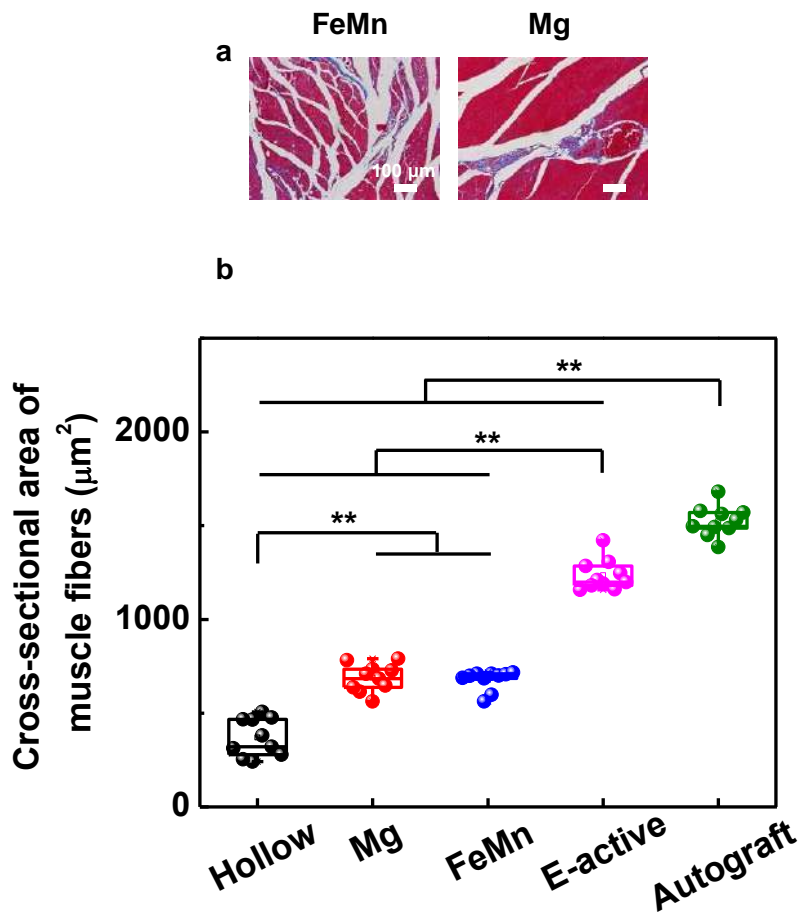


Figure S24. Ultrasound elasticity of gastrocnemius muscles from the injured limb at 12 weeks postimplantation.  $n = 5$  independent animals per group. The SPSS software package (version 23.0) was used for the statistical analysis followed by ANOVA (\*  $p < 0.05$ , \*\*  $p < 0.01$ ).



**Figure S25. Evaluation of the gastrocnemius muscle at 12 weeks postimplantation.** **a.** Gross images of the isolated gastrocnemius muscles of the FeMn and Mg groups. **b.** Gastrocnemius muscle wet weight ratio from the injured limb.  $n = 5$  independent animals per group. The SPSS software package (version 23.0) was used for the statistical analysis followed by ANOVA (\*  $p < 0.05$ , \*\*  $p < 0.01$ ). Photo Credit: Changfeng Lu, Chinese PLA General Hospital.



**Figure S26. Evaluation of the gastrocnemius muscle at 12 weeks postimplantation.** **a.** Masson's trichrome staining images of the transverse sections of the muscles from the injured limb of the FeMn and Mg groups. **b.** Cross-sectional area of muscle fiber from the injured limb.  $n = 5$  independent animals per group. The SPSS software package (version 23.0) was used for the statistical analysis followed by ANOVA (\*\*  $p < 0.01$ ).

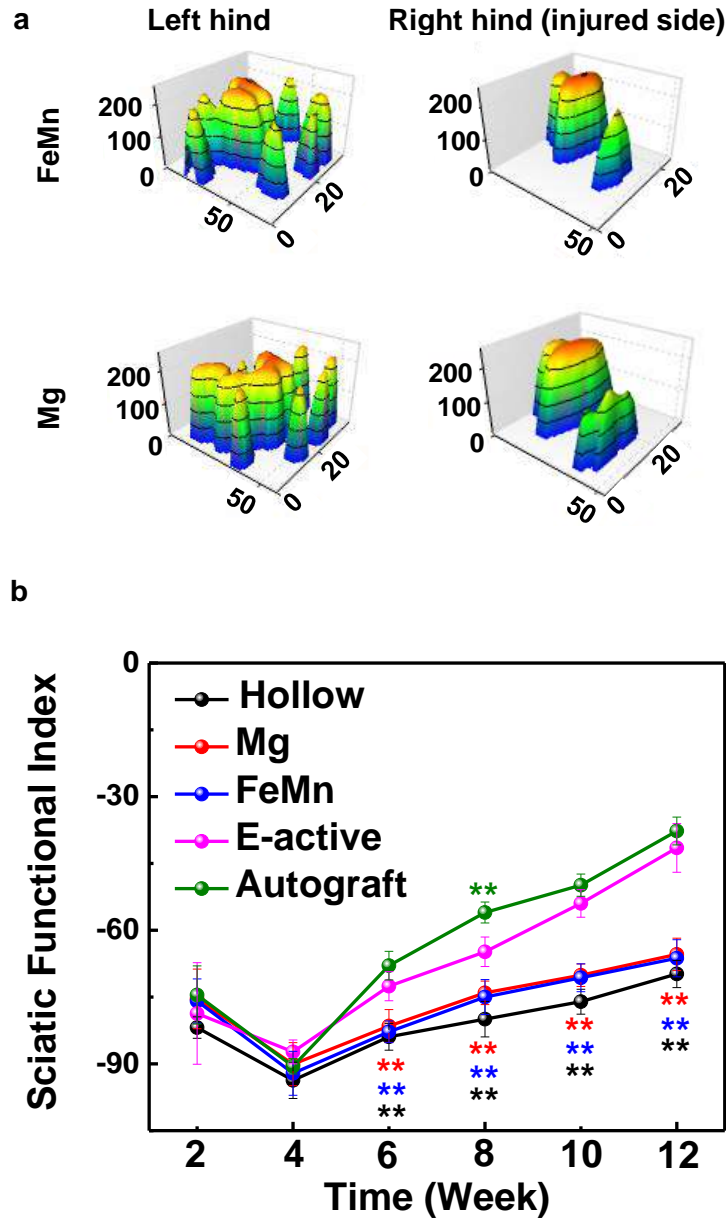


**Figure S27. Motor functional recovery.** **a.** 3D plantar pressure distribution at 12 weeks postimplantation of the FeMn and Mg groups. **b.** Sciatic functional index values. (data are mean  $\pm$  s. d.) For each group,  $n = 11$  for week 2,  $n = 8$  for week 4, 6 and 8, and  $n = 5$  for week 10 and 12. The SPSS software package (version 23.0) was used for the statistical analysis followed by ANOVA (\*\*  $p < 0.01$  versus E-active group).

**Table S1. ELISA of neurotrophic factors: the concentrations of BDNF, CNTF, NGF and VEGF in the supernatants of Schwann cells of all groups.**

<b>Group</b>	<b>BDNF (ng/ml)</b>	<b>CNTF (ng/ml)</b>	<b>NGF (pg/ml)</b>	<b>VEGF (pg/ml)</b>
Control	6.3 ± 1.06	8.8 ± 0.78	97.5 ± 4.17	103.3 ± 2.57
FeMn	15.8 ± 1.30	15.3 ± 0.35	230.5 ± 9.45	160.3 ± 2.4
Mg	18.0 ± 1.21	16.4 ± 0.53	232.4 ± 7.51	167.2 ± 6.9
E-active	19.5± 0.37	23.7± 1.40	351.1± 12.91	202.9±13.30

**Movie S1. Calcium dynamics of DRG neurons in the control group.**

**Movie S2. Calcium dynamics of DRG neurons in the E-active group.**

**Movie S3. Surgical procedure of the implantation of an electroactive conduit device at the sciatic nerves of an SD rat.**

**Movie S4. Motor functional recovery: walking track of SD rats at 12 weeks postimplantation. Right hind (RH) limb is the injured side.**